energies

MDPI

Article

Permeability Evolution and Water-Rock Reaction Mechanism of Dolomite Geothermal Reservoirs in Wumishan Formation During Reinjection

Haoyang Chen [1], Bo Feng [1], Chong Li [2,3,*], Zhenxing Li [2,3], Heqing Lei [1], Zheng Liu [1] and Qing Liu [4]

[1] Engineering Research Center of Geothermal Resources Development Technology and Equipment, Ministry of Education, Jilin University, Changchun 130026, China; haoyangc25@mails.jlu.edu.cn (H.C.); fengbo82@126.com (B.F.); leihq23333@126.com (H.L.); 15148857683@163.com (Z.L.)
[2] Hebei Key Laboratory of Precision Exploration Technology for Deep Geothermal Resources, Xiongan 070001, China; lb23010013@cumt.edu.cn
[3] Hydrogeology Bureau of China National Administration of Coal Geology, Xiongan 070001, China
[4] Beijing Institute of Geothermal Research, Beijing 100012, China; 13041264088@163.com
* Correspondence: lb22010014@cumt.edu.cn

Abstract

Geothermal reinjection is critical for sustainable exploitation of geothermal resources, yet the permeability evolution mechanism of carbonate geothermal reservoirs remains poorly understood. Taking dolomite geothermal reservoirs of the Wumishan Formation in the Xiong'an New Area as the research object, high-temperature and high-pressure dynamic flow experiments and TOUGHREACT simulations were performed to investigate the effects of injection pressure, temperature, and water chemistry on the permeability of matrix and fractured cores. Results show that the optimal injection pressure and temperature for both core types are 14 MPa and 70 °C. Under such conditions, the final average permeability of matrix and fractured cores is 0.0015 mD and 0.0287 mD, with CV values of 7.3% and 6.2%, respectively. Chemically treated water suppresses calcite dissolution by altering ionic composition and pH, thereby reducing permeability of both cores, while the reduction is less significant for fractured cores. Simulations indicate that reinjection water triggers slightly stronger calcite dissolution than dolomite precipitation and yields permeability enhancement. When treated water is injected, reaction intensity declines, Mg^{2+} concentration approaches zero, and dolomite precipitation becomes more thorough. Matrix cores follow an "activation-stabilization" pattern, whereas fractured cores exhibit a "decay-convergence" pattern and are more sensitive to pressure. This study reveals distinct responses of matrix and fractures to hydrochemical perturbations in dual-porosity carbonate geothermal reservoirs, demonstrating that permeability evolution during reinjection is jointly governed by reservoir pore type and hydrochemical conditions. The findings provide mechanistic support for targeted regulation of reinjection water chemistry.

Keywords: geothermal reinjection; Wumishan Formation; dolomite geothermal reservoirs; permeability evolution; water-rock reaction; dynamic seepage experiment; core-scale numerical simulation

Check for updates

Academic Editor: Reza Rezaee

Received: 23 September 2026
Revised: 19 October 2026
Accepted: 20 October 2026
Published: 25 October 2026

Copyright: © 2026 by the authors. Licensee MDPI, Basel, Switzerland. This article is an open access article distributed under the terms and conditions of the Creative Commons Attribution (CC BY) license.

1. Introduction

Geothermal reinjection serves as a key measure for sustainable exploitation of geothermal resources. Reinjection of spent thermal water into geothermal reservoirs maintains reservoir pressure and guarantees production capacity, and has been widely applied in

global geothermal development [1–5]. Nevertheless, a core challenge exists in reinjection engineering practice: injected fluids differ substantially from in-situ geothermal fluids in temperature, pressure, and chemical composition. Such differences inevitably disturb the water-rock equilibrium within reservoirs, trigger mineral dissolution or precipitation, and thereby alter the flow capacity of geothermal reservoirs [6,7]. This dynamic evolution of flow capacity directly restricts reinjection efficiency and long-term safety. For dolomite geothermal reservoirs of the Jixianian Wumishan Formation widely distributed in northern China, the problem becomes particularly complex, as their reservoir pore space consists of matrix pores and fracture networks [8–10]. The two media differ by orders of magnitude in hydraulic properties. Many studies, however, simplify geothermal reservoirs as homogeneous media [11–13], failing to identify whether matrix and fracture zones follow identical flow evolution laws during reinjection, nor to clarify the dominant mechanisms underlying their divergent responses. Building on this background, the present study focuses on how matrix pores and fracture networks respond differently under reinjection conditions in the Wumishan Formation.

We hypothesize that, owing to their contrasting flow velocities, residence times, and reactive surface areas, matrix pores and fracture networks respond differently to the same injected water: fractures, with short residence time and small reactive surface, undergo limited mineral reaction and are dominated by mechanical effects; the matrix, with long residence time and large surface area, hosts more pronounced water-rock interaction and a stronger permeability response to water chemistry.

In seepage research of fractured media, artificially split cores have been widely adopted to construct controllable fracture channels [14,15]. This method can effectively separate the seepage contributions of fractures and matrix, providing an experimental basis for quantitative evaluation of fracture conductivity [16]. It should be noted that hydraulic properties differ between artificial and natural fractures. Artificial fractures feature rougher surfaces and simpler geometry, and their permeability is generally more sensitive to effective stress than natural fractures [15,17]. Nevertheless, recent comparative studies suggest that such differences exert limited impacts on flow behavior [15,18]. Therefore, although artificially split cores cannot fully reproduce the heterogeneity of natural fracture networks, the fracture-dominated seepage mechanisms revealed under controlled conditions still offer mechanistic references for understanding the divergent responses of dual-porosity geothermal reservoirs [19,20]. Fresh split surfaces may also have artificially high mineral reactivity and lack the infilling and alteration layers typical of natural karst fractures; tests on cores with natural microfractures or pre-conditioned surfaces are recommended for future work.

Regarding permeability evolution of geothermal reservoirs, numerous experiments have been conducted on thermal effects [21–23], pressure effects [24], and coupled thermo-hydro-mechanical effects [25,26], revealing permeability sensitivity to temperature and pressure variations. For water-rock reactions, the combined approach of laboratory experiments and geochemical simulations (e.g., PHREEQC, TOUGHREACT) has been successfully applied to identify mineral dissolution-precipitation patterns during reinjection [6,27–31], clarify migration and transformation pathways of key ions [32–35], and predict dynamic permeability responses under multi-physics coupling conditions [12,35–38]. Despite abundant achievements, existing studies generally simplify reservoirs as homogeneous cores. Few controlled experiments systematically compare seepage responses between matrix and fracture zones under identical temperature, pressure, and water chemistry conditions. Furthermore, the temporal linkage mechanism between real-time evolution of hydrochemical parameters and dynamic permeability changes has not been fully established. This hinders the identification of which water-rock reactions, within which reservoir pore spaces,

dominate the degradation or enhancement of reinjection capacity. A methodological feature of this study is the combined use of experimental and simulation approaches, with the experiments ensuring the overall accuracy of the reaction–permeability linkage and the simulations providing a refined characterization of its temporal correlation.

Alkalization with Na_2CO_3/NaOH and chelation with citric acid have been used in prior laboratory studies as a water-treatment recipe for geothermal reinjection water, mainly to reduce Ca/Mg hardness and inhibit Fe(III) oxide precipitation. The specific recipe tested here follows the static-batch experimental setup of [34]; however, that earlier work examined only aqueous chemistry under static conditions and did not measure permeability evolution. Whether such chemical conditioning alters in-situ water-rock reactions and matrix/fracture permeability under dynamic flow and reservoir temperature-pressure conditions has not been characterized, which motivates the original-vs-treated water comparison in the present study. To further investigate this issue, this study takes dolomite geothermal reservoirs of the Jixianian Wumishan Formation as the research object and designs comparative dynamic seepage experiments using matrix cores and artificially split cores. By setting different injection pressures, core temperatures, and hydrochemical compositions of injected water, real-time permeability monitoring and outlet fluid sampling are performed to capture differences in seepage response characteristics between the two types of cores under the above variables. On this basis, combined with core-scale numerical simulation, the divergent evolution behaviors and internal mechanisms of matrix pores and fracture networks driven by reinjection fluids are revealed from the perspective of water-rock reaction pathways. This provides a basis for in-depth understanding of water-rock reaction processes in heterogeneous carbonate geothermal reservoirs. The primary goal of this study is to reveal the coupled permeability evolution and water-rock reaction mechanisms in dual-porosity dolomite geothermal reservoirs during reinjection, with four secondary objectives: (1) optimal pressure/temperature conditions; (2) matrix-vs-fracture response differences; (3) water-chemistry regulation paths; and (4) TOUGHREACT validation.

2. Study Area and Geothermal Setting

The study area is located in the Rongcheng Bulge structural zone of Xiong'an New Area, with its specific location shown in Figure 1. The Rongcheng Bulge lies in the northern Jizhong Depression of the North China Basin, serving as a secondary uplifted structural unit adjacent to structural units including the Xushui Sag and Niutozhen Bulge. The major fault zone composed of the Rongcheng East Fault and Niunan Fault provides space and channels for the storage and thermal convection of geothermal water in the study area [39].

The primary geothermal reservoir in the study area is the dolomite geothermal reservoir of the Jixianian Wumishan Formation [39]. As a typical carbonate geothermal reservoir, it mainly occurs in the Rongcheng Bulge, Niutozhen Bulge, and the intermediate sub-sag. Its lithology is dominated by grayish-white and gray-brown argillaceous dolomite [40]. The formation of this geothermal reservoir is closely related to tectonic activities. Tectonic uplift during the Yanshanian–Himalayan orogenies and long-term leaching generated abundant karst fractures favorable for reservoir development [41]. The top boundary of the Wumishan Formation geothermal reservoir in this area is relatively shallow, generally ranging from 700 to 2200 m, with a thickness of 300–1000 m. The reservoir thickness ratio exceeds 20%, and the average porosity is 3.18% [39,42,43]. The Cenozoic caprock directly overlies the Wumishan Formation dolomite and provides effective thermal insulation.

The average heat flow value of the Rongcheng Bulge reaches 74.2 mW/m^2, representing a high-anomaly area [42,44]. Geothermal water is primarily derived from meteoric precipitation in the Taihang and Yanshan Mountains. It flows along faults and unconformities and is continuously heated by deep heat sources during migration and accumulation, forming a

hydrothermal geothermal system. The Wumishan Formation geothermal reservoir in the Rongcheng Bulge is well fractured, with coexisting matrix pores and fracture networks. It exhibits typical dual-medium characteristics, making it an ideal candidate for comparative seepage experiments of matrix-pore and fracture dual media [42].

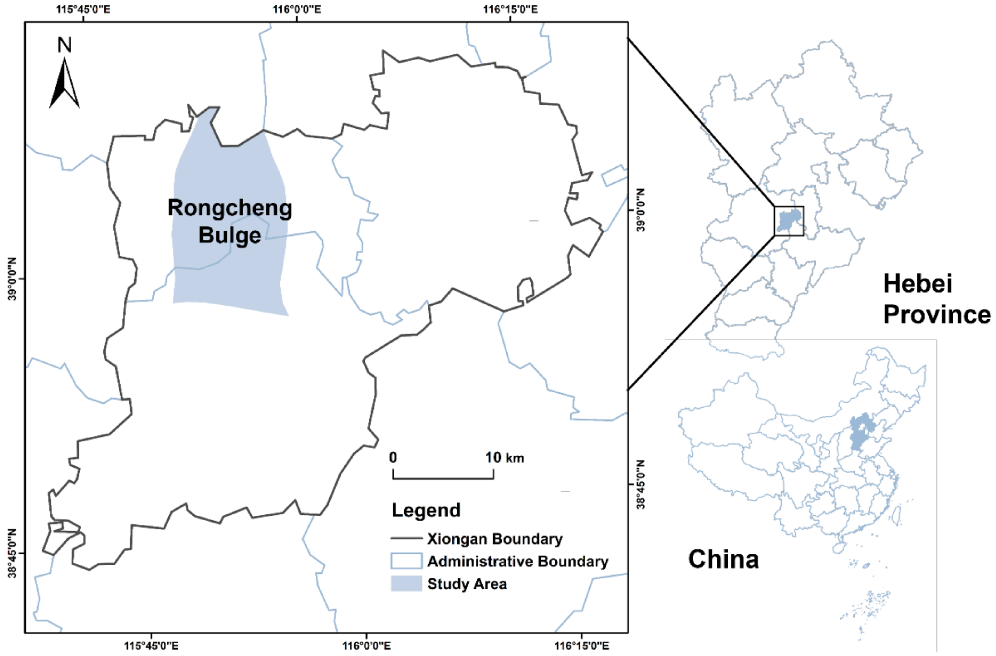


Figure 1. Location map of the study area.

3. Dynamic Seepage Experiment

3.1. Sample Collection and Pretreatment

3.1.1. Water Sampling and Pretreatment

Water samples in this study were collected from geothermal reinjection water at Satellite Station 4-3 in the Rongdong area, Xiong'an New Area. To investigate the effects of injected water chemistry conditions on core permeability and water-rock reaction, the collected geothermal reinjection water was divided into two treatment groups. One portion of the water samples was only filtered through 5 μm and 0.45 μm membranes to remove suspended solids without altering pH and ionic composition, defined as representative reinjection water (hereafter referred to as original water). The other portion was chemically treated: biocide was first added to eliminate microorganisms, followed by filtration using a 5 μm membrane. Subsequently, 0.18 g/L Na_2CO_3, 0.25 g/L NaOH, and 25 mL citric acid were added to the filtrate, and the solution was filtered through a 0.45 μm membrane to obtain chemically treated water (hereafter referred to as treated water).

The above treatment scheme was designed based on the following considerations: Na_2CO_3 and NaOH are common hardness removers for geothermal reinjection water, which have been adopted at both laboratory [34] and field [45] scales. As an organic complexing agent, citric acid can adjust pH, dissolve iron-bearing carbonate cements, enhance rock porosity and permeability, and inhibit the precipitation of Fe(III) oxides in porous media [46].

3.1.2. Rock Sampling and Pretreatment

Rock samples for the experiments were collected from outcrops of the Jixianian Wumishan Formation in Tianjin. X-ray diffraction (XRD) results show that the mineral composition is dominated by dolomite, with a mass fraction of approximately 83%, followed by calcite

(15%) and talc (2%). The diffraction pattern is presented in Figure 2. Physical property tests indicate that the gas permeability of all rock samples ranges from 0.2 to 0.3 mD. These data were used for core consistency evaluation and grouping. The water-phase permeability obtained from dynamic experiments was adopted uniformly in subsequent permeability evolution analysis. Five core samples (numbered 1–5) were used in this study. Their gas permeabilities measured in the intact state before fracturing are 0.2861, 0.2860, 0.2830, 0.2587, and 0.2667 mD (mean = 0.276 mD, CV = 4.6%), confirming that the tested cores are highly comparable. Cores 1–4 were used as matrix cores; core 4 was further used for the temperature and water-chemistry groups. Core 5 was artificially split to serve as the fractured core, and its listed gas permeability was measured before splitting.

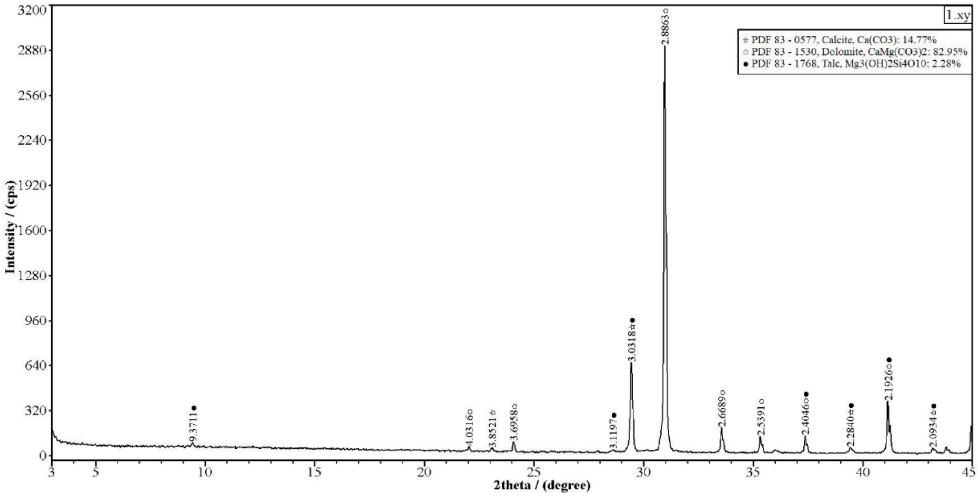


Figure 2. XRD patterns of rock samples.

The rock samples were collected from surface outcrops and have undergone long-term supergene weathering. Their pore structures may differ from those of deep in-situ geothermal reservoirs, so it is necessary to evaluate their representativeness. Previous studies have systematically analyzed reservoir characteristics of the Wumishan Formation in the Rongcheng Bulge, Xiong'an New Area. The results reveal that the Wumishan Formation geothermal reservoir in this area is mainly composed of crystalline dolomite, grain dolomite, and microbial dolomite, with dolomite as the dominant mineral [43], which is similar to the mineral composition of the rock samples used in this study. In terms of physical properties, the Wumishan Formation geothermal reservoir has an average porosity of 3.18% and permeability of 91.48×10^{-3} μm^2 [43]. These values are of the same order of magnitude as the measured data of our rock samples. Although the absolute physical properties of outcrop samples may deviate slightly due to weathering, their low-porosity and low-permeability matrix properties and pore scale are comparable to the matrix section of in-situ geothermal reservoirs. Therefore, dynamic seepage experiments performed on these outcrop samples can provide reliable experimental evidence for understanding the coupled seepage-reaction behavior of matrix pores in Wumishan Formation dolomite. We note, however, that long-term weathering may have altered mineral surface reactivity and that absolute dissolution-precipitation rates measured here may differ quantitatively from the deep reservoir; future tests on fresh deep drill cores are needed to verify this.

Rock samples were cut and machined into cylindrical specimens with uniform dimensions of approximately 25 mm in diameter and 50 mm in height. Half of these specimens were split using a dedicated fracture-making machine to create artificial fractures, serving as fractured cores. The remaining specimens were kept as matrix cores. Photographs of selected cores are shown in Figure 3.



Figure 3. Photographs of selected matrix cores and fractured cores.

Static dissolution tests using treated water were performed on the rock to evaluate the representativeness of the split surface involved in water-rock interaction. The SEM images before and after the reaction are displayed in Figure 4. Before reaction (Figure 4a), dolomite crystals show intact morphology, and calcite fills intergranular spaces. After reaction (Figure 4b), calcite is preferentially dissolved to form dissolution pores; dolomite surfaces exhibit dissolution features with abundant secondary mineral precipitation. These results indicate that the rock exhibits obvious water-rock interaction activity upon contact with fluids. As fresh fracture surfaces, artificial split surfaces can trigger water-rock interaction dominated by calcite dissolution under dynamic seepage conditions. Without infilling minerals and alteration layers existing in natural fractures, artificial split surfaces may have higher reactivity than natural fracture surfaces. In addition, the split surfaces have simple geometry and cannot reflect complex reaction behaviors at fracture intersections within natural fracture networks. Therefore, conclusions on fracture reactions derived from split cores in this study should be regarded as mechanistic references rather than direct quantitative extrapolation of reaction magnitudes for field fracture networks. We note that SEM provides localized 2D surface imaging; future work using pre- and post-test micro-CT scanning would enable 3D visualization and quantification of internal pore-throat dissolution channels, particle migration, and secondary mineral precipitation within the core volume.

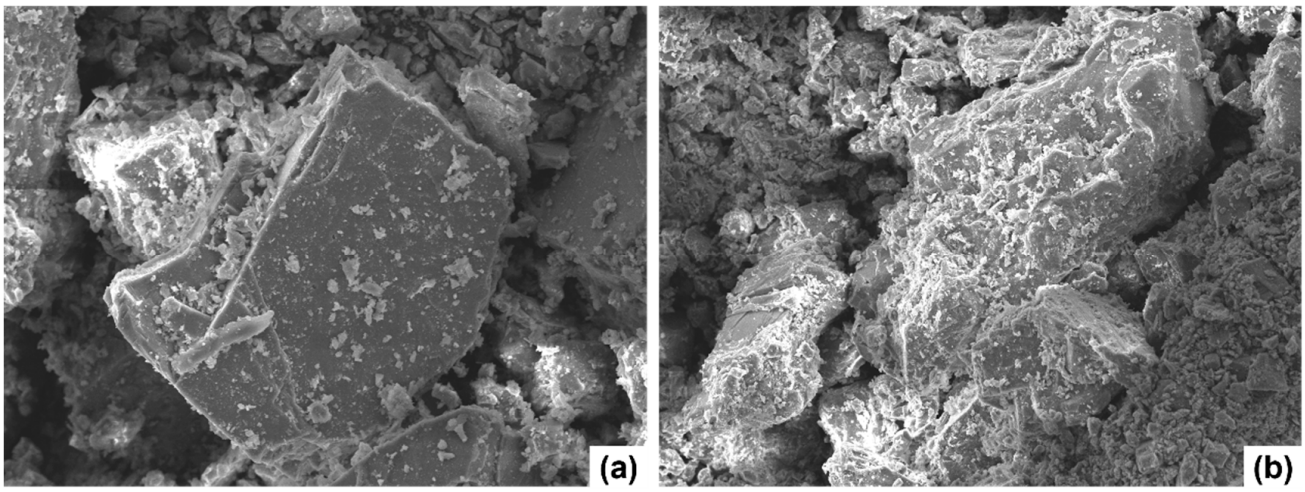


Figure 4. SEM images of the sample: (**a**) before reaction; (**b**) after reaction.

3.2. Experimental Principle and Apparatus

The formula for calculating core permeability (Equation (1)) was derived based on Darcy's law, the liquid pressure formula, and the conversion relationship between permeability and hydraulic conductivity.

$$k = \frac{Q\mu L}{A(P_1 - P_2)}, \quad (1)$$

where k is the core permeability (m^2), Q is the volumetric flow rate ($m^3 \cdot s^{-1}$), μ is the dynamic viscosity (Pa·s), L is the core length (m), A is the core cross-sectional area (m^2), P_1 is the inlet pressure (Pa), and P_2 is the outlet pressure (Pa).

Considering that the total dissolved solids (TDS) of both original water and treated water are less than 2.8 g/L, these waters are classified as low-mineralized water. The deviation of their viscosity from pure water is acceptable for engineering calculations [47]. Therefore, the dynamic viscosity values of pure water at corresponding temperatures were adopted (Table 1).

Table 1. Viscosity of pure water at different temperatures.

Temperature (°C)	70	80	90
Viscosity (mPa·s)	0.404	0.356	0.317

A self-developed high-temperature and high-pressure dynamic flow apparatus (Figure 5) was used in the experiments. The instrument mainly consists of a constant-pressure and constant-flux pump, a thermostatic oven, a core holder, and a hand pump. The injected fluid is delivered by the constant-pressure and constant-flux pump into the core inside the core holder. A confining pressure valve and a thermostatic oven are used to simulate actual formation conditions. After reaction, the fluid is cooled in a condenser and then flows into the solution collector placed on an electronic balance to measure the volumetric flow rate Q.

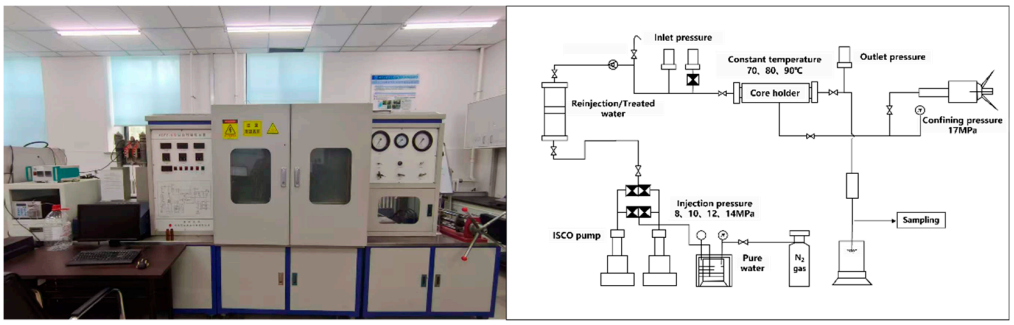


Figure 5. Schematic and photograph of the high-temperature and high-pressure dynamic seepage apparatus.

The following measures were adopted in this study to guarantee data reliability: the cores were fully vacuum-saturated prior to experiments; the core-jacket interface was tightly sealed to eliminate bypass flow; and the effective axial flow was assumed to pass through the entire cross-sectional area.

3.3. Experimental Design

To systematically analyze the effects of injection pressure, temperature, and water chemistry conditions on seepage characteristics of dolomite geothermal reservoirs, three groups of progressive dynamic seepage experiments were designed with a fixed confining

pressure of 17 MPa (Table 2), considering the effective sealing of the core-jacket interface and in-situ stress measurement results of the shallow strata in Xiong'an New Area [48]. Experiments D-09 and D-12 in the temperature group reused partial data from the injection pressure group, while experiments D-15 and D-16 in the water chemistry group reused partial data from the temperature group. Note that under this fixed confining pressure, varying the injection pressure from 8 to 14 MPa corresponds to a reduction of the effective stress from 9 to 3 MPa; the injection-pressure group therefore couples mechanical (effective-stress) and chemical (water-rock reaction) contributions, whose separation is addressed explicitly in Section 5.

Table 2. Experimental scheme.

ID	Type	Fluid	Temp. (°C)	Core No.	Initial Gas k (mD)	Pressure (MPa)
D-01	Matrix	Original	70	1	0.2861	8
D-02	Matrix	Original	70	2	0.2860	10
D-03	Matrix	Original	70	3	0.2830	12
D-04	Matrix	Original	70	4	0.2587	14
D-05	Fractured	Original	70	5	0.2667	8
D-06	Fractured	Original	70	5	0.2667	10
D-07	Fractured	Original	70	5	0.2667	12
D-08	Fractured	Original	70	5	0.2667	14
D-09	Matrix	Original	70	4	0.2587	14 (Optimal)
D-10	Matrix	Original	80	4	0.2587	14 (Optimal)
D-11	Matrix	Original	90	4	0.2587	14 (Optimal)
D-12	Fractured	Original	70	5	0.2667	14 (Optimal)
D-13	Fractured	Original	80	5	0.2667	14 (Optimal)
D-14	Fractured	Original	90	5	0.2667	14 (Optimal)
D-15	Matrix	Original	70 (Optimal)	4	0.2587	14 (Optimal)
D-16	Fractured	Original	70 (Optimal)	5	0.2667	14 (Optimal)
D-17	Matrix	Treated	70 (Optimal)	4	0.2587	14 (Optimal)
D-18	Fractured	Treated	70 (Optimal)	5	0.2667	14 (Optimal)

Note: Matrix, matrix core; Fractured, fractured core; Original, original water; Treated, treated water. Optimal pressure (14 MPa) and optimal temperature (70 °C) were determined from the injection pressure group and temperature group, respectively.

The permeability of matrix cores differs from that of fractured cores by approximately two orders of magnitude, leading to a substantial difference in seepage response time. In steady-state permeability measurements, low-permeability cores require much longer time to achieve stable pressure and flow rate than high-permeability cores. Previous studies have indicated that steady-state tests for tight rocks may take several days to weeks [49]. To ensure fair comparisons among different working conditions for the same core type and considering the time required for permeability to reach relative stability in each test group, a unified experimental cut-off time was set separately for the two types of cores in this study: 2500 min for matrix cores and 150 min for fractured cores.

For all working conditions, the moving average of permeability over the final 10% time interval was adopted as the representative value of each condition, denoted as the end-stage average permeability (k_{end}), for cross-comparison among different working conditions. This data selection follows the general principle of "averaging data from the steady-state segment" in steady-state permeability measurements [50]. The final 10% time interval is a reasonable choice given the dataset size in this study, and the moving average within this window can effectively eliminate random fluctuations. We acknowledge that fractured-core runs were shorter (approximately 150 min) than matrix runs (approximately 2500 min)

because of the higher flow rate; although permeability had converged by the end of the fractured runs, longer experiments or equalized cumulative pore volumes would more rigorously confirm long-term geochemical steady state, and this is noted as a direction for future work.

Permeability stability was quantitatively evaluated using the coefficient of variation (CV):

$$CV = \frac{\sigma}{k_{\text{end}}} \times 100\%, \quad (2)$$

where σ is the standard deviation of data within the end-stage window. CV is a dimensionless index; a smaller value indicates weaker fluctuations.

Referring to the classification logic of CV for reservoir heterogeneity evaluation [51], and considering that this study assesses the temporal fluctuation of permeability for a single core under one working condition, the evaluation criteria were defined as follows: CV < 10% represents a stable state, 10–20% represents moderate fluctuation, and >20% represents severe fluctuation.

3.4. Experimental Results and Analysis

3.4.1. Injection Pressure Group

For the injection pressure group, the permeability evolution characteristics of matrix cores and fractured cores under 8–14 MPa are shown in Figure 6. The end-stage average permeability and coefficient of variation for each working condition are summarized in Table 3.

Table 3. Permeability evolution characteristics of cores under different injection pressures.

Core Type	8 MPa	10 MPa	12 MPa	14 MPa
Matrix core, k_{end} (mD)	0.0010	0.0013	0.0017	0.0015
Matrix core, CV (%)	41.7	13.0	46.0	7.3
Fractured core, k_{end} (mD)	0.0148	0.0223	0.0191	0.0287
Fractured core, CV (%)	17.6	19.2	18.3	6.2

The permeability of matrix cores generally exhibits a characteristic pattern of "rapid initial rise—fluctuating adjustment in the middle stage—gradual stabilization in the later stage". At 8 MPa and 10 MPa, the end-stage average permeability values are 0.0010 mD and 0.0013 mD with CV values of 41.7% and 13.0%, respectively. The maximum average permeability (0.0017 mD) occurs at 12 MPa, while the corresponding CV reaches 46.0%, indicating an unstable system. At 14 MPa, the average permeability is 0.0015 mD, and the CV is only 7.3%, which is the only stable test among the four groups. The analysis suggests that the high permeability and strong fluctuation at 12 MPa originate from the enhanced pore connectivity driven by elevated pressure, accompanied by particle migration and alternating plugging-breakthrough of pore throats. At 14 MPa, the flow channels can be kept stably open, leading to converged fluctuations.

The permeability of fractured cores shows a pattern of "rapid initial decay—gradual stabilization in the later stage", which is distinctly different from that of matrix cores. The end-stage average permeability values are 0.0148, 0.0223, 0.0191 and 0.0287 mD at 8, 10, 12 and 14 MPa, respectively. The CV at 14 MPa is only 6.2%, representing the best stability among the four tests. Fractured cores exhibit no "activation" stage because high-conductivity channels already exist and do not require pressure for opening. Pressure only counteracts the mechanical closure of fracture surfaces. At 14 MPa, the inhibition of closure by effective stress is the most sufficient, leading to the slowest permeability decay and the optimal steady state.

Combining the results of the two core types, 14 MPa was determined as the common optimal injection pressure for both matrix and fractured cores.

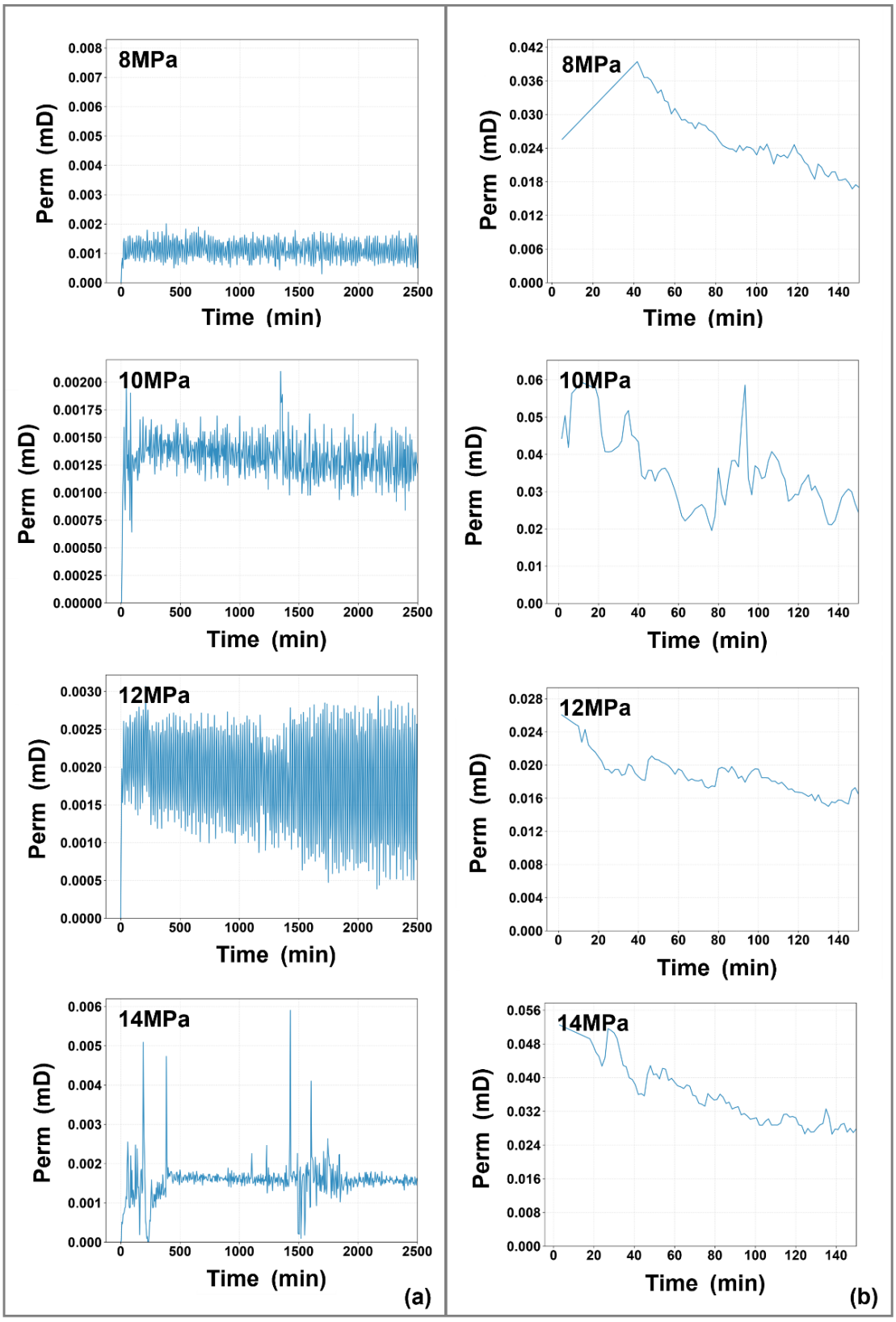


Figure 6. Permeability–time curves of matrix and fractured cores in the injection pressure group: (**a**) matrix core; (**b**) artificially fractured core.

3.4.2. Temperature Group

In the temperature group experiments, the permeability evolution characteristics of matrix cores and fractured cores at 70, 80, and 90 °C are illustrated in Figure 7. The end-stage average permeability and coefficient of variation under each working condition are summarized in Table 4.

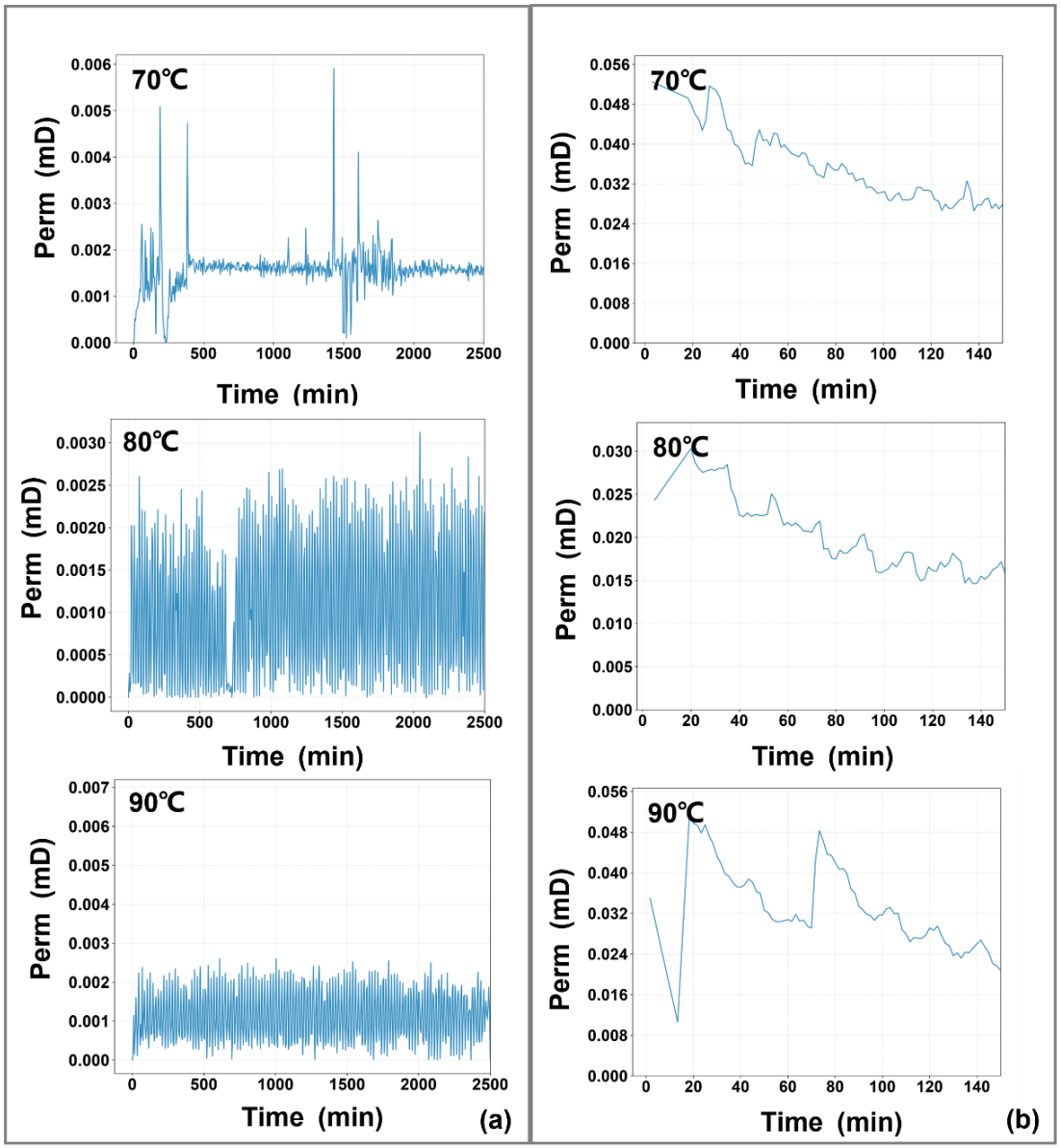


Figure 7. Permeability–time curves for the temperature group: (**a**) matrix core; (**b**) artificially fractured core.

Table 4. Permeability evolution characteristics of cores at different temperatures.

Core Type	70 °C	80 °C	90 °C
Matrix core, k_{end} (mD)	0.0015	0.0012	0.0015
Matrix core, CV (%)	7.3	76.0	65.9
Fractured core, k_{end} (mD)	0.0287	0.0156	0.0246
Fractured core, CV (%)	6.2	12.6	7.2

For matrix cores, the end-stage average permeability is 0.0015 mD with a CV of only 7.3% at 70 °C, showing the best stability. At 80 °C, the average permeability decreases to 0.0012 mD and the CV reaches 76.0%, indicating severe permeability degradation and violent oscillation. At 90 °C, the average permeability returns to 0.0015 mD, but the CV rises to 65.9%, with abrupt increases and instability in the later stage. The analysis reveals that above 70 °C, temperature elevation accelerates mineral dissolution and substantially increases carbonate supersaturation. Consequently, permeability enhancement by dissolution and permeability reduction by precipitation alternately dominate the process, leading to frequent plugging and breakthrough of pore throats.

For fractured cores, the end-stage average permeability reaches the maximum value of 0.0287 mD with a CV of only 6.2% at 70 °C. At 80 °C, the end-stage average permeability drops to the minimum value of 0.0156 mD and the CV increases to 12.6%, corresponding to rapid permeability decay. At 90 °C, the end-stage average permeability is 0.0246 mD, and the CV is 7.2%; the system undergoes violent oscillation (alternating closure and breakthrough) in the early stage and gradually stabilizes in the later stage. Owing to the short fluid residence time, the water-rock reaction extent of fractured cores is lower than that of matrix cores, which weakens the promoting effect of high temperature on chemical precipitation. The high-temperature instability of fractured cores mainly arises from thermally induced stress that intensifies the alternating mechanical closure and opening of fracture surfaces, rather than chemical oscillation.

Combining the results of the two core types, 70 °C was determined as the common optimal core temperature for both matrix and fractured cores.

3.4.3. Water Chemistry Group

In the water chemistry group experiments, the permeability evolution characteristics of the two core types under original water and treated water are shown in Figure 8. The end-stage average permeability and coefficient of variation under each working condition are summarized in Table 5.

Table 5. Permeability evolution characteristics of cores under different injected water chemistry.

Core Type	Original Water	Treated Water
Matrix core, k_{end} (mD)	0.0015	0.0011
Matrix core, CV (%)	7.3	32.2
Fractured core, k_{end} (mD)	0.0287	0.0252
Fractured core, CV (%)	6.2	5.3

For matrix cores, the end-stage average permeability is 0.0015 mD with CV = 7.3% under original water, showing a stable curve. Under treated water, the end-stage average permeability decreases to 0.0011 mD with CV = 32.2%, exhibiting persistent high-frequency oscillation. The permeability for treated water is approximately 27% lower than that for original water. Treated water inhibits the natural dissolution of calcite and weakens the self-enhancing mechanism of "dissolution-induced permeability increase". Meanwhile, the high-pH environment promotes the precipitation of secondary minerals at pore throats, resulting in reduced permeability and intensified fluctuations.

For fractured cores, the end-stage average permeability is 0.0287 mD with CV = 6.2% under original water, presenting convergence after steady decay. Under treated water, the end-stage average permeability is 0.0252 mD with CV = 5.3%, and a sharp pulsed fluctuation occurs in the middle stage. The permeability for treated water is about 12% lower than that for original water. The reduction in fractures is smaller than that in the matrix because of the fast fluid velocity and short reaction contact time, which weaken the chemical inhibition

effect. Nevertheless, fractures serve as dominant flow channels, and the 12% permeability reduction still deserves attention at the engineering scale.

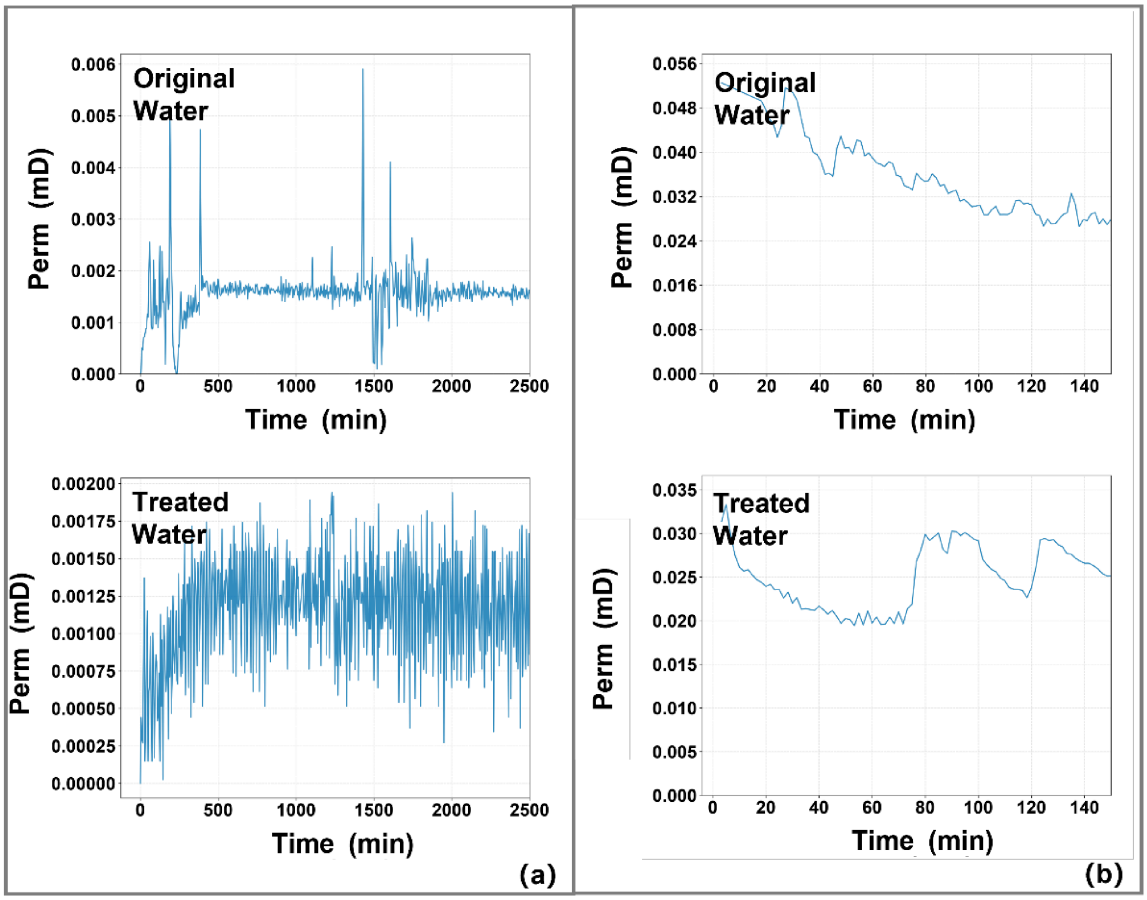


Figure 8. Permeability–time curves for the water chemistry group: (**a**) matrix core; (**b**) artificially fractured core.

Combining the results of the two core types, original water was identified as the optimal injected water for both matrix and fractured cores.

The differences in permeability variations indicate distinct water-rock reaction pathways between the two injected fluids and rock. However, permeability alone cannot directly reveal the direction and magnitude of reactions. To interpret the mechanisms behind different permeability responses, the measured water chemistry data should be further analyzed to provide chemical evidence for permeability evolution.

The effluent water collected at the outlet from the water chemistry group and the two injected fluids were tested, and their pH values and major ion concentrations are shown in Figure 9.

In terms of injected fluids, the measured pH of original water is 8.27, and that of treated water is 8.97; the pH of treated water is slightly higher than that of original water. The variation trends of outlet pH differ under the two injected water types. After injection of original water, the outlet pH rises from the inlet value of 8.27 to 8.93 and 8.80 for matrix cores and artificially fractured cores, respectively. After injection of treated water, the outlet pH decreases from the inlet value of 8.97 to 8.64 and 8.81 for matrix cores and artificially fractured cores, respectively.

In terms of ion concentrations, the concentrations of Ca^{2+} and Mg^{2+} at the outlet decrease for both core types when treated water is used, and the reduction is more remarkable in matrix cores (Ca^{2+} decreases from 38.3 to 8.33 mg/L, a reduction of 78%; Mg^{2+} decreases

from 26.6 to 14.0 mg/L, a reduction of 47%). The HCO_3^- concentration slightly decreases in matrix cores (358.5 to 310.2 mg/L) and slightly increases in fractured cores (524.8 to 548.6 mg/L).

Overall, although treated water has a higher inlet pH, its outlet pH after injection is still lower than the inlet value, accompanied by substantial reductions in Ca^{2+} and Mg^{2+} concentrations. This indicates that treated water inhibits the dissolution of carbonate minerals and weakens the positive feedback mechanism of "leaching-induced permeability increase".

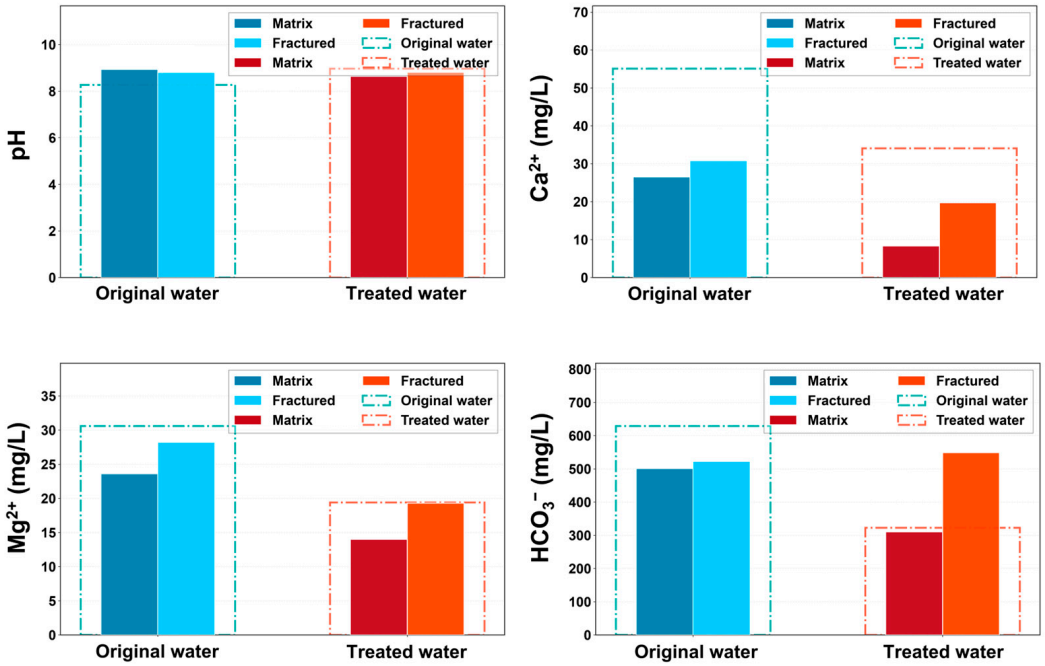


Figure 9. Bar charts of pH and major ion concentrations.

4. Core-Scale Numerical Simulation

4.1. Core Model

TOUGHREACT was adopted in this study for core-scale modeling. Since the core temperature can be maintained by the thermostatic oven, the EOS1 module was selected to simulate the seepage-reaction process of cores under single-phase and isothermal conditions. A hydrogeochemical (HC) coupled flow-chemistry core model was established with reference to key parameters including rock mineral composition measured by XRD and permeability obtained from seepage experiments.

4.2. Boundary and Initial Conditions

Constant-pressure control was applied for flow boundaries. The injection end pressure was set to 140 bar and the outlet pressure to 1 bar to drive the unidirectional seepage of single-phase water from the injection end to the outlet. The entire core was kept at a constant temperature of 70 °C, and the injected fluid shared the same temperature. The outer wall of the core was defined as an adiabatic boundary with no heat exchange with the surrounding environment. At the initial time, the pore space of the core was water-saturated; the hydrodynamic field and temperature field were consistent with the boundary conditions and remained unchanged during the simulation.

4.3. Mesh Discretization

The simulated object is a cylindrical dolomite core with a diameter of 25 mm and a height of 50 mm. Structured meshes in the three-dimensional Cartesian coordinate system

were adopted, and the core was approximated as a cylinder with an approximately circular cross-section of equal height, whose volume is basically consistent with that of the original cylindrical core. The z-direction (flow direction) was discretized into 20 layers with a height of 2.5 mm for each layer. Restricted by the circular cross-section, the number of meshes in the x and y directions ranges from 7 to 25. Uniform meshes were used for matrix cores, with a total mesh number of 9780 (Figure 10a). To maintain consistency with experimental samples, local mesh refinement was performed at the central position (the 12th column of meshes in the x-direction) for fractured cores. The refined mesh size is approximately one-tenth of that of the other meshes to characterize the physical properties of fractures, and the total mesh number reaches 9860 (Figure 10b).

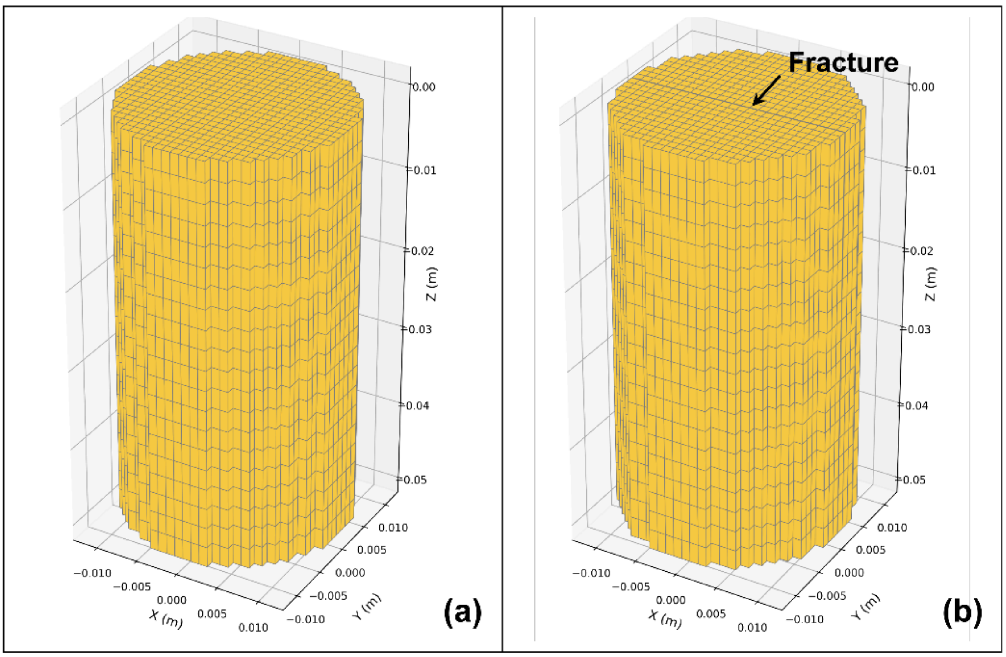


Figure 10. Schematic diagram of core mesh discretization: (**a**) matrix core, (**b**) fractured core.

4.4. Core Parameters

The permeability of the rock matrix is 1.7×10^{-18} m^2, approximately equal to 0.0017 mD. This value is close to the maximum end-stage average permeability of matrix cores in the experiments, which can better reflect the effect of water-rock reaction on core permeability and is reasonably adopted as the initial rock permeability. The initial porosity is 0.02, and the grain density is 2600 kg/m^3. Permeability was dynamically updated with mineral dissolution–precipitation during simulation. Since the permeability variation is less than 1%, it can be neglected; therefore, permeability changes were set to have no feedback on reaction kinetic calculations.

Fracture permeability was estimated based on the cubic law (Equation (3)).

$$k = \frac{b^2}{12}, \tag{3}$$

Considering the widespread development of microfractures in carbonates of the Wumishan Formation within the study area, the hydraulic fracture aperture was assumed to be 0.01 mm in this study. This assumption is consistent with the typical aperture range of microfractures in regional carbonate rocks [52]. The permeability calculated by the cubic law is approximately 8.33×10^{-12} m^2. The equivalent permeability of grids containing fractures was estimated by volume weighting, yielding an equivalent permeability of approximately 8.33×10^{-13} m^2, namely 844 mD. The validity of this law has been experimentally verified for

various rock types (granite, basalt, marble, etc.) and aperture ranges (0.004–0.25 mm) and is independent of rock type [53]. Note that the 844 mD is the volume-weighted permeability of fracture-containing grids, not the core-scale equivalent permeability; these differ by the fracture-to-total volume ratio in the dual-porosity model. The 0.01 mm aperture follows the typical microfracture aperture range of regional carbonates and is used for reactive surface-area assignment rather than as a calibrated hydraulic match.

Mineral compositions are expressed as volume fractions: dolomite 0.83, calcite 0.15, and the remaining 0.02 represents inert minerals. The initial pore water chemistry was obtained by pre-simulating the reaction between original water and dolomite for 10 years at 70 °C and 170 bar to bring the initial state close to mineral saturation. The measured chemical compositions of original water and treated water were adopted for the injected fluid at the injection boundary, respectively.

4.5. Geochemical Parameters

The dissolution–precipitation reactions of dolomite, calcite, and gypsum were considered, and all were controlled by reaction kinetics. The mineral dissolution–precipitation rate was calculated using the general rate expression built in TOUGHREACT [54]:

$$r_n = k_n A_n \left(1 - \frac{Q}{K}\right), \tag{4}$$

where r_n is the mineral reaction rate ($mol \cdot m^{-3} \cdot s^{-1}$); positive values indicate dissolution and negative values indicate precipitation. k_n is the rate constant ($mol \cdot m^{-3} \cdot s^{-1}$); A_n is the specific reactive surface area (m^2/m^3); Q is the ion activity product; and K is the equilibrium constant. The temperature dependence of the rate constant k_n was corrected by the Arrhenius equation:

$$k_n = k_{25} \backslash exp\left[-\frac{E_a}{R\left(\frac{1}{T} - \frac{1}{298.15}\right)}\right], \tag{5}$$

where k_{25} is the rate constant at 25 °C ($mol \cdot m^{-2} \cdot s^{-1}$); E_a is the activation energy ($kJ \cdot mol^{-1}$); R is the gas constant (8.314×10^{-3} $kJ \cdot mol^{-1} \cdot K^{-1}$); and T is the absolute temperature (K).

The kinetic parameters of the three minerals adopt the recommended values from the built-in database of TOUGHREACT [54]: for calcite, $k_{25} = 6.4565 \times 10^{-7}$ $mol/(m^2 \cdot s)$, $E_a = 62.76$ kJ/mol; for dolomite, $k_{25} = 1.2589 \times 10^{-9}$ $mol/(m^2 \cdot s)$, $E_a = 62.76$ kJ/mol; for gypsum, $k_{25} = 1.91 \times 10^{-4}$ $mol/(m^2 \cdot s)$, $E_a = 18.98$ kJ/mol. The pH dependence was realized via an acid-catalyzed mechanism: the reaction order $n = 1.0$ for pH ≤ 4, $n = 0.5$ for pH ≥ 8, with a linear transition in the intermediate range. We note that the reactive surface area (An) was assigned based on typical literature values rather than measured BET specific surface area for these specific dolomite samples; calibrating An with measured BET data would improve the quantitative accuracy of simulated effluent ion concentrations.

4.6. Simulation Scheme Design

The total simulation duration is 3 days for matrix cores and 3 h for fractured cores. An initial time step of 0.001 s was adopted to capture the early variations in chemical gradients, followed by automatic time-step growth without maximum step-size limitation. Results were output at every time step to track the evolution of minerals, water chemistry, and porosity.

To match the experimental working conditions, four simulation cases were designed (Table 6), corresponding to the seepage-reaction processes of the two core types under two injected water chemistries in the water chemistry group. The injected water chemistry, core type, temperature, and pressure conditions of the four simulation cases are consistent with those in the water chemistry group experiments.

Table 6. Setup of numerical simulation cases.

Case ID	Experiment	Core Type	Fluid	Duration
Case 1	D-15	Matrix core	Original water	3d
Case 2	D-16	Fractured core	Original water	3h
Case 3	D-17	Matrix core	Treated water	3d
Case 4	D-18	Fractured core	Treated water	3h

Note: Matrix, matrix core; Fractured, fractured core; Original, original water; Treated, treated water; d, days; h, hours.

4.7. Simulation Results and Analysis

4.7.1. Spatial and Temporal Evolution of pH and Ion Concentrations

The pH–time distributions at the core outlet for the four simulation cases are shown in Figure 11. Since Cases 2 and 4 adopt the fractured core model containing both matrix and fracture domains with substantial differences, their results are presented separately. In the figure, R and F represent the matrix domain and fracture domain of the core, respectively. When original water is injected, the overall pH of the core column continuously decreases from the initial value of 7.4 to approximately 5.9. The pH evolves more slowly in fractures than in the matrix and finally converges. When treated water is injected, the pH exhibits a trend of initial decline followed by a rise and finally rebounds to approximately 7.0.

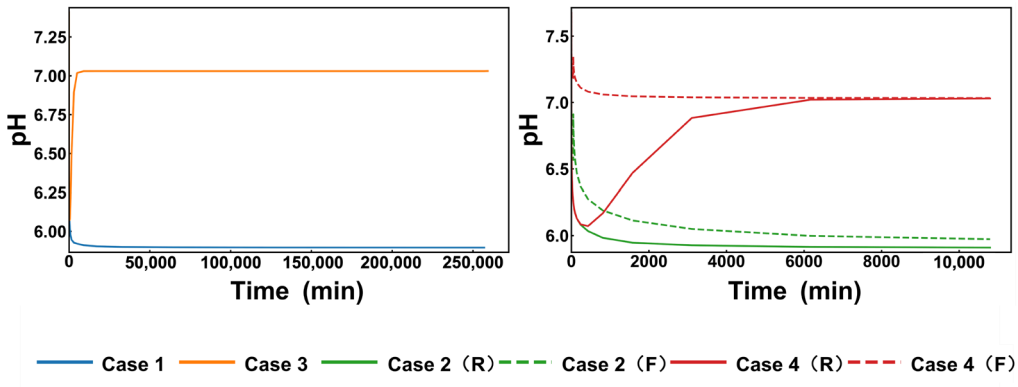


Figure 11. pH–time curves (R: matrix domain; F: fracture domain of the core).

The calcium ion concentration (Figure 12) continuously rises during injection of original water. For Case 1, the overall concentration increases to approximately 0.036 mol/L. In Case 2, the concentration increment in fractures is always lower than that in the matrix. For treated water injection, the calcium concentration exhibits an initial rise followed by a decline. In Case 3, the concentration rises to 0.028 mol/L and then decreases to 0.001 mol/L. The matrix domain in Case 4 shows a similar trend to Case 3, while the fracture domain undergoes a smaller variation. The two domains eventually converge to the same value.

The magnesium ion concentration (Figure 13) shows a continuous decreasing trend in all four simulation cases. The two cases with original water injection decrease to approximately 0.004–0.006 mol/L, while the two cases with treated water injection drop to nearly 0 mol/L, indicating a more thorough reaction. The reduction of Mg^{2+} in fractures is smaller than that in the matrix, which is especially prominent in Case 2. The concentration remains at approximately 0.014 mol/L in fractures, whereas it decreases to 0.004 mol/L in the matrix.

The bicarbonate concentration (Figure 14) exhibits an initial decline followed by a rise in all four simulation cases. Cases 1 and 2 finally rebound to approximately 0.0065 mol/L, while Cases 3 and 4 rebound to a low level of 0.005 mol/L.

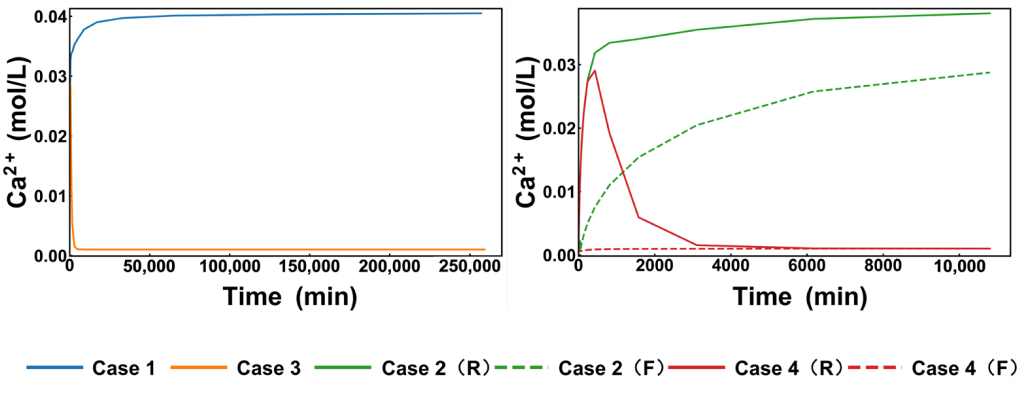


Figure 12. Calcium ion concentration–time curves (R: matrix domain; F: fracture domain of the core).

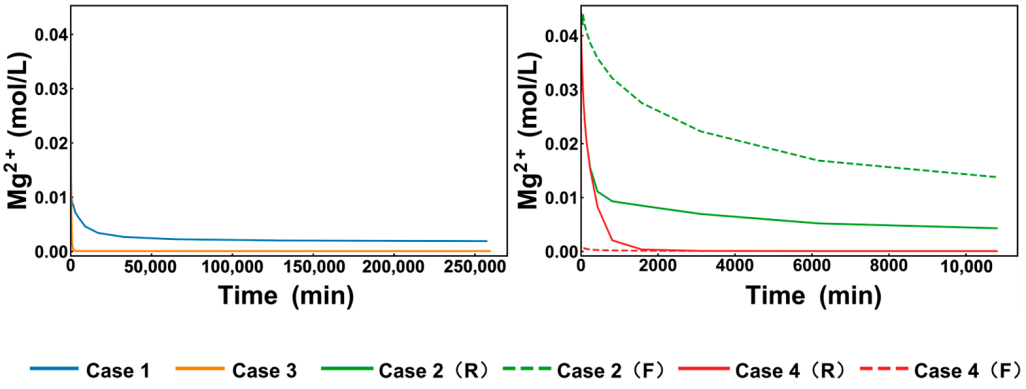


Figure 13. Magnesium ion concentration–time curves (R: matrix domain; F: fracture domain of the core).

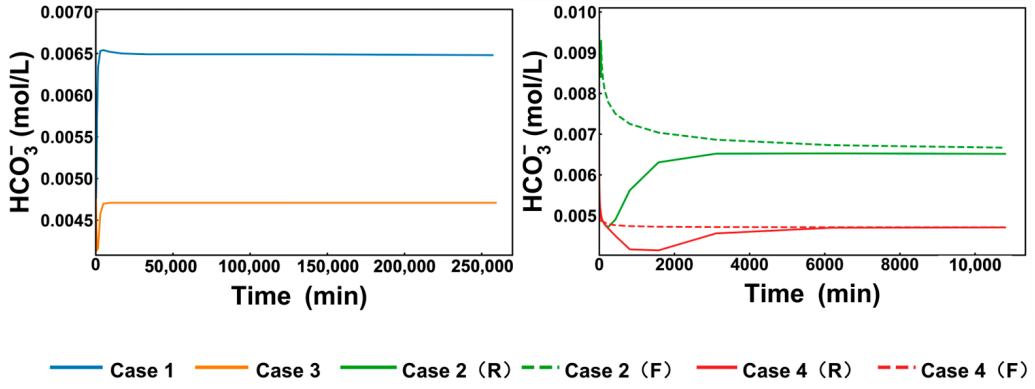


Figure 14. Bicarbonate concentration–time curves (R: matrix domain; F: fracture domain of the core).

The above ion evolution trends indicate that the system is dominated by calcite dissolution when original water is injected. The continuous increase of Ca^{2+} and the trend of initial decline followed by rebound for HCO_3^- reflect the balance between consumption and replenishment during dissolution. By contrast, dissolution is inhibited, and dolomite precipitation dominates after treated water injection, with Mg^{2+} approaching zero. The key factor responsible for this remarkable difference is the pH of injected fluids. The variation amplitude in fractures is smaller than that in the matrix, mainly owing to the high fluid velocity and short reaction contact time, which lead to incomplete water-rock reaction.

4.7.2. Variations in Mineral Content

Variations in mineral content are expressed as the differences in volume fraction between the final simulation time and the initial state; positive values represent precipitation, and negative values represent dissolution. The spatial distributions of volume fraction changes for calcite and dolomite at the end of the four simulation cases are illustrated in Figure 15. Although gypsum dissolution and precipitation were considered in the geochemical parameter setup of the model, no gypsum reactions were observed in the output results, and thus gypsum is not presented here.

Calcite dissolution and dolomite precipitation occur in all four simulation cases. The reaction extent is larger under original water injection than under treated water injection. In Case 1, calcite decreases by 0.0005–0.0007 and dolomite increases by 0.0005–0.0006. In Case 2, the variation magnitude in the matrix is approximately half that in Case 1, while the variation magnitude in fractures is 3–5 times that in the matrix. The reaction extents in Cases 3 and 4 are obviously smaller than those in Cases 1 and 2 with original water injection. The mineral content varies more rapidly in fractures than in the matrix. These observations reveal that Ca^{2+} is supplied by calcite dissolution, which drives dolomite precipitation. For the cases with original water injection, calcite dissolution proceeds more sufficiently, and the amount of dolomite precipitation is greater.

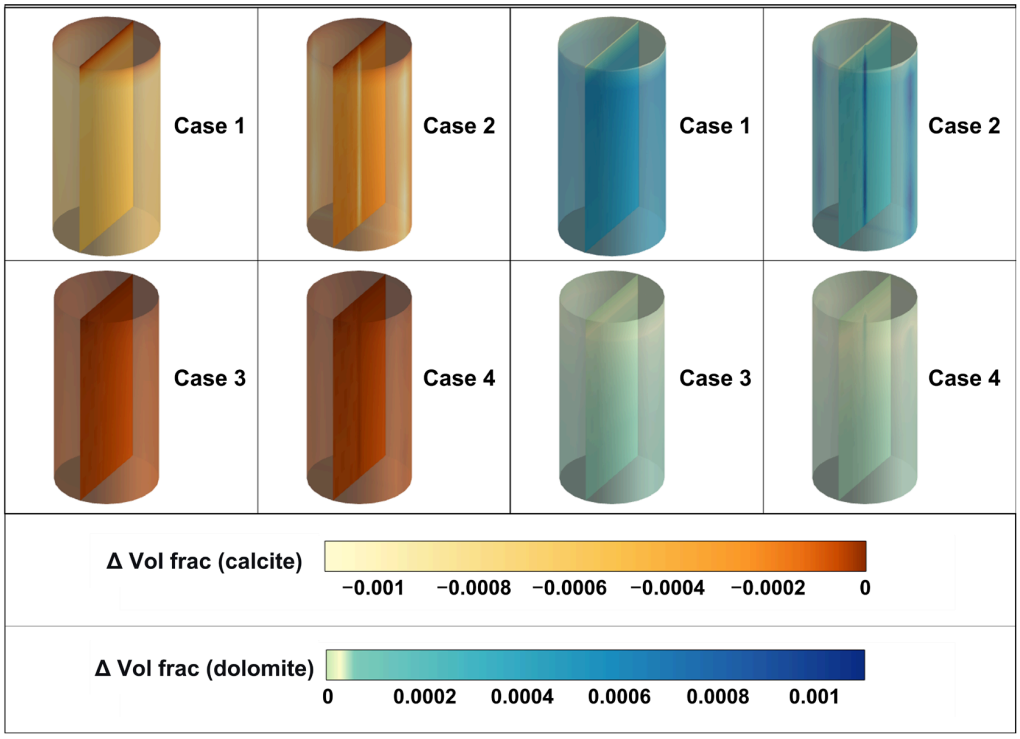


Figure 15. Spatial distribution of mineral volume fraction variations at the end of each simulation case.

4.7.3. Permeability Variation

The spatial distributions of core permeability at the end of the four simulation cases (Figure 16) show that longitudinally, the permeability of the matrix domain increases under original water injection. For Case 1, the permeability rises by 0.69–0.78%, and for Case 2, the permeability increases by 0.3–0.38%. For treated water injection, the matrix domain exhibits both permeability increase and decrease, with variations ranging from −0.06% to 0.04%. In contrast, the permeability of fracture domains in Cases 2 and 4 slightly decreases, with reduction magnitudes of 0.06–0.09%.

The temporal evolution of permeability at the outlet (Figure 17) indicates that the permeability of the matrix domain continuously rises for the original water cases. For treated water cases, the matrix domain shows minor variation with a slight increase. The fracture domain presents an initial decline followed by a rise (Case 2) or continuous reduction (Case 4). Horizontally, for matrix cores, the permeability of Case 3 is 0.58% lower than that of Case 1. For fractured cores, the matrix domain of Case 4 decreases by 0.23% compared with Case 2, and the fracture domain decreases by 0.02%.

The direction of permeability variation is positively correlated with the net mineral dissolution amount, confirming that permeability responses in the simulation are governed by the dissolution–precipitation equilibrium. The measured outlet pH (8.64–8.93) is 1.6–3.0 units higher than the simulated value (5.9–7.0). The dominant cause is CO_2 degassing upon cooling of the outlet fluid to room temperature, which raises measured pH but is not represented in the isothermal 70 C TOUGHREACT run; a secondary contribution is the pre-equilibrated initial pore water (pH 7.4) versus the water initially filling the core. For permeability, the measured reduction under treated water (27% matrix, 12% fractured) exceeds the simulated prediction (0.58%, 0.23%) because the model only accounts for mineral-volume change, whereas measured evolution also includes effective-stress fracture closure and particle migration. Despite these offsets, trends agree: original water yields slight calcite dissolution and permeability enhancement, treated water suppresses dissolution and drives precipitation.

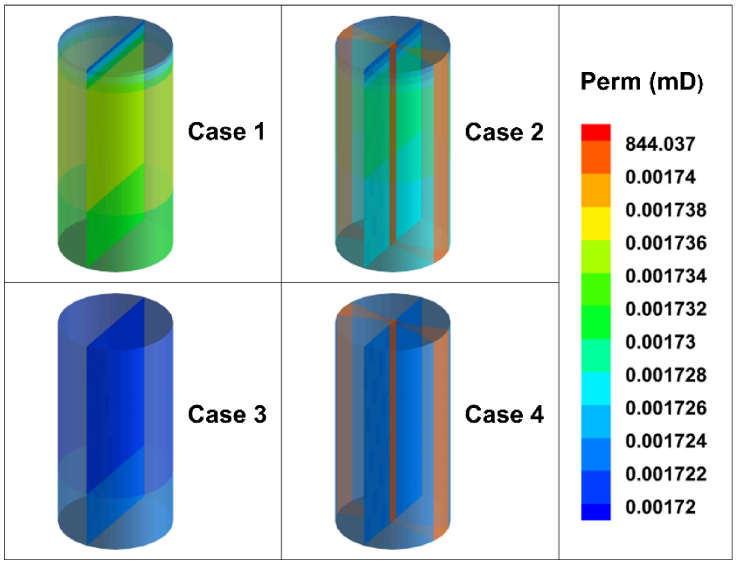


Figure 16. Spatial distribution of permeability at the end of each simulation case.

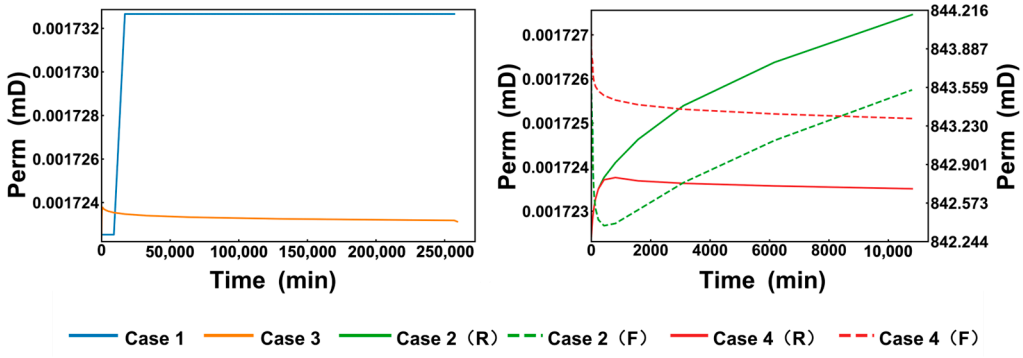


Figure 17. Permeability–time curves at the outlet for each simulation case.

5. Discussion

5.1. Regulation Mechanism of Injected Water Chemistry for Water-Rock Reaction Paths

By comparing the hydrochemical and permeability responses between the two groups of experiments using original water and treated water, the regulation direction and magnitude of water quality variation on water-rock reactions can be identified. Original water retains the chemical composition of the initial geothermal fluid and represents the natural hydrochemical background within the geothermal reservoir. Treated water is prepared by artificially adding Na_2CO_3, NaOH, and citric acid to modify pH, ionic strength, and carbonate ion activity. Parallel comparison of these two water types forms the experimental basis for revealing the coupled hydrochemistry–permeability mechanism.

Ion concentration data from the experiments first indicate differences in reaction paths. For matrix cores, the outlet Ca^{2+} concentration is 38.3 mg/L after injection of original water, while it decreases to 8.33 mg/L after injection of treated water, a reduction of approximately 78%. The Mg^{2+} concentration decreases from 26.6 mg/L to 14.0 mg/L, a reduction of approximately 47%. This difference demonstrates that treated water markedly inhibits the dissolution of calcite and dolomite. The measured pH of treated water is 8.97, higher than the value of 8.27 for original water, whereas the concentrations of Ca^{2+} and Mg^{2+} decline due to dilution and precipitation. These comprehensive variations in ionic composition jointly shift the equilibrium position of mineral dissolution–precipitation.

Differences in permeability fluctuation characteristics also support this mechanistic analysis. For matrix cores, the CV value is 7.3% under original water conditions, corresponding to a "stable" level, while it rises to 32.2% under treated water conditions, representing "violent fluctuation". This indicates that treated water does not induce uniform and gradual permeability reduction; instead, it triggers an unsteady state characterized by alternating opening and clogging of pore throats. The most plausible explanation is that changes in the water chemistry of treated water alter the chemical environment on pore surfaces and the direction of mineral reactions, promoting the generation and accumulation of secondary minerals and resulting in the observed high-frequency oscillations. This interpretation is also consistent with the experimental and simulation results that the permeability reduction is larger in matrix cores than in fractured cores. The tortuous and complex pore network of the matrix provides more trapping sites than the relatively straight fracture channels.

In summary, the comparison between original water and treated water enables identification of how variations in injected water chemistry regulate water-rock reaction paths. A weak positive feedback of "leaching and permeability enhancement" exists under the original hydrochemical condition. In contrast, alkaline treated water inhibits calcite dissolution and shifts the reaction equilibrium, weakening this feedback and introducing the risk of secondary mineral precipitation. This mechanistic understanding provides experimental constraints for interpreting the coupling relationship between water chemistry and permeability.

5.2. Insights into Dual-Porosity Geothermal Reservoirs from Matrix–Fracture Differences

The parallel experimental design of matrix and fractured cores provides a unique perspective for understanding the differentiated behaviors of the two types of storage-seepage spaces, which offers direct implications for the understanding and management of dolomite dual-porosity geothermal reservoirs.

The fundamental difference lies in the magnitude of permeability. Under identical conditions (14 MPa, 70 °C, original water), the permeability of fractured cores is approximately 20 times that of matrix cores (0.0287 mD vs. 0.0015 mD). This discrepancy is expected; however, of greater importance than the magnitude itself is the differentiated response of the two media to pressure and hydrochemical perturbations.

Under different injection pressures, matrix cores exhibit an "activation–stabilization" pattern: permeability rises rapidly in the early stage and then stabilizes, with the optimal performance achieved at 14 MPa (CV = 7.3%). By contrast, fractured cores show a "decay–convergence" pattern: permeability peaks at the initial stage and then gradually declines to a steady level. This difference indicates that the dominant processes governing the two systems are fundamentally distinct. In the matrix, injection pressure drives the opening of originally isolated pores and forms flow channels; this is a one-time activation process that remains stable once completed. In fractures, injection pressure mainly counteracts the mechanical closure of fracture surfaces. Fracture surfaces tend to continuously converge under effective stress. Even at 14 MPa, persistent slow permeability decay was observed for fractured cores, implying that partial fracture closure proceeds and a true steady state may not be reached within the experimental time.

The two systems differ in their sensitivity to water chemistry. The outlet permeability of fractured cores in the treated water group is approximately 12% lower than that in the original water group, while the reduction reaches approximately 27% for matrix cores. This reveals that fractures exhibit a relatively weak response to hydrochemical variations. Numerical simulations provide mechanistic interpretation for this phenomenon: the fluid residence time in fractures is markedly shorter than that in the matrix. The rate of Mg^{2+} decline and the increment of Ca^{2+} in fracture grids are both lower than those in matrix grids. The limited contact duration between injected fluids and mineral surfaces reduces the extent of water-rock reaction.

It should be noted that the matrix injection-pressure group (D-01 to D-04) used four independent cores (cores 1–4, initial gas permeability 0.2587–0.2861 mD, CV = 4.6%), whereas the temperature group, water-chemistry group, and all fractured-core tests were conducted on a single core (core 4 for matrix, core 5 for fractures) under sequentially varied conditions. This design was chosen deliberately: for fractured cores, testing all conditions on one split core eliminates inter-sample variability in fracture geometry and roughness; for matrix cores, the 14 MPa/70 C condition was set as the anchor and subsequent temperature/water-chemistry variations were performed on the same core to isolate each variable. The trade-off is that earlier reaction history may carry over to later runs; this is mitigated by re-measuring the anchor condition in multiple groups (D-04, D-09, D-15). In addition, gas permeability and aqueous permeability differ by several orders of magnitude. Therefore, the absolute values of 12% and 27% may incorporate contributions from sequential reaction history rather than inter-sample variability (because the anchor and subsequent conditions shared the same core), and should not be extrapolated as precise quantitative estimates of water chemistry effects. Nevertheless, ion concentration data demonstrate that treated water substantially suppresses the release of Ca^{2+} and Mg^{2+}, and the permeability of both core types is lower under treated water than under original water. Multiple lines of evidence are consistent in terms of trend. Accordingly, the conclusion that treated water alters water-rock reaction paths and affects permeability evolution is qualitatively reliable.

The above findings indicate that reinjection management strategies for dual-porosity geothermal reservoirs should consider dominant flow pathways. For fracture-dominated geothermal reservoirs such as the Wumishan Formation, maintaining sufficient injection pressure to resist fracture closure is the primary concern, while hydrochemical treatment plays a secondary yet non-negligible role. For matrix-dominated geothermal reservoirs, emphasis should be placed on preserving the natural dissolution-enhancing mechanism that helps sustain pore connectivity.

Effective-stress and water-rock contributions are coupled in the injection-pressure group because the confining pressure was held at 17 MPa while injection pressure varied from 8 to 14 MPa, which simultaneously lowered effective stress from 9 to 3 MPa. We

separate the two contributions as follows. (1) The steady-state permeability contrast across pressures (e.g., fractured cores at ~0.029 mD under 14 MPa versus ~0.015 mD under 8 MPa) is dominated by the mechanical response: higher injection pressure directly counteracts fracture-face closure under effective stress, an essentially instantaneous response consistent with the strong stress-sensitivity of artificially split fractures. (2) The time-dependent drift within a single run–rising permeability in matrix cores, sustained slow decay in fractured cores, and oscillation at 90 C–occurs over hundreds to thousands of minutes, far beyond the seconds-to-minutes timescale of poro-elastic deformation, and is therefore attributed to water-rock reactions. (3) The water-chemistry control runs, performed at identical 14 MPa and 70 C but with different injected water, isolate the chemical contribution under fixed effective stress: switching from original water to treated water reduced permeability by approximately 12% in fractured cores and 27% in matrix cores. (4) The TOUGHREACT simulations independently capture the direction of chemically driven permeability change (slight enhancement under original water, inhibition and possible precipitation under treated water). Taken together, the across-pressure contrast mainly reflects effective-stress mechanics, whereas the within-run evolution and the water-chemistry contrast are attributable to water-rock reactions.

5.3. Engineering Implications for Sustainable Geothermal Reinjection in the Xiong'an New Area

By comparing the two groups with original water and treated water, the core finding of this study is that artificially modifying the chemical composition of injected water (increasing pH, raising carbonate and sulfate concentrations, and reducing Ca and Mg concentrations) substantially alters water-rock reaction paths. Calcite dissolution is inhibited, the magnitude of dolomite precipitation is modified, and the permeability response shifts from a "stable" state to "violent fluctuation". The significance of this result lies in the demonstration that chemical adjustment of reinjection water can materially modify water-rock reactions within the reservoir. The consequences of such modification can only be predicted with a thorough understanding of the reactive characteristics of the target reservoir.

Under experimental conditions, original water exhibits a more stable capacity for permeability maintenance than treated water. This does not mean that original water is always superior. Instead, it indicates that a dynamic equilibrium has been established between the natural hydrochemical environment and rocks for this reservoir, and artificially breaking this equilibrium may trigger unintended consequences. The reductions in Ca^{2+} and Mg^{2+} concentrations and the rise in pH within treated water collectively shift the mineral dissolution–precipitation equilibrium and weaken the naturally existing weak positive feedback of leaching and permeability enhancement.

Based on the above understanding, for the reinjected water chemistry management of Wumishan Formation dolomite geothermal reservoirs in the Xiong'an New Area, substantial chemical conditioning of reinjection water should not be casually implemented before fully characterizing the water-rock reaction features of the reservoir. This conclusion is derived from the specific treatment scheme adopted in this study, namely alkalization conditioning by adding Na_2CO_3, NaOH, and citric acid after filtration. Other types of chemical treatments may exert different effects on water-rock reaction paths, and their performance must be evaluated via targeted experiments. Accordingly, the above conclusion is limited to alkalization conditioning schemes similar to the experimental setup in this work and cannot be directly extended to all reinjection water treatment processes.

More broadly, by comparing the two injected water chemistries, this study provides experimental evidence and numerical simulation validation for understanding how hydrochemical variations drive the coupling between mineral reactions and permeability in

carbonate geothermal reservoirs. The research methodology can serve as a reference for reinjection water chemistry assessment of analogous geothermal reservoirs.

6. Conclusions

This study targets the dolomite geothermal reservoir of the Jixian Wumishan Formation in the Xiong'an New Area. High-temperature and high-pressure dynamic seepage experiments and TOUGHREACT numerical simulations were conducted to investigate the effects of injection pressure, temperature, and injected water chemistry on permeability evolution and water-rock reactions of matrix and fractured cores. The main conclusions are drawn as follows:

1. The optimal injection pressure and temperature for the two core types under experimental conditions were determined. The optimal injection pressure is 14 MPa and the optimal injection temperature is 70 °C for both matrix and fractured cores. Under these conditions, the average permeability at the outlet of the matrix core is 0.0015 mD with CV = 7.3%, while the average permeability at the outlet of the fractured core is 0.0287 mD with CV = 6.2%.
2. The regulation mechanism of injected water chemistry variation on water-rock reaction paths is revealed. Comparative experiments between original water and chemically treated water demonstrate that treated water modifies the ionic composition and pH of the solution, inhibits calcite dissolution, and alters the magnitude of dolomite precipitation, shifting the permeability response from a stable state (CV = 7.3%) to violent fluctuation (CV = 32.2%). Numerical simulations further show that calcite dissolution slightly exceeds dolomite precipitation during original water injection, resulting in permeability enhancement. By contrast, the overall reaction intensity decreases under treated water injection, and Mg^{2+} approaches zero, indicating more thorough dolomite precipitation. These results demonstrate that artificially modifying the chemical composition of injected water can substantially alter water-rock reaction paths within the reservoir, and additional alkalization and carbonate addition may induce unintended shifts in reaction pathways.
3. The differentiated responses of matrix pores and fractures, two types of storage-seepage spaces, to hydrochemical and pressure perturbations are clarified. Fractured cores are less sensitive to hydrochemical variations than matrix cores owing to short fluid residence time and incomplete water-rock reaction. Nevertheless, fractured cores are more sensitive to pressure changes. At 14 MPa, the average outlet permeability (0.0287 mD) is approximately twice the value at 8 MPa (0.0148 mD). Matrix cores follow an "activation–stabilization" pattern, whereas fractured cores exhibit a "decay–convergence" pattern. These differences can provide references for reinjection management of dual-porosity geothermal reservoirs. We note that this roughly twofold across-pressure contrast contains a dominant effective-stress contribution rather than purely chemical effects; the chemical contribution under fixed effective stress is instead quantified by the water-chemistry control described in Section 5.

Author Contributions: Conceptualization, H.C., B.F. and C.L.; methodology, H.C. and Z.L. (Zhenxing Li); software, H.C. and Q.L.; validation, B.F. and H.L.; formal analysis, H.C. and Z.L. (Zheng Liu); investigation, H.C. and H.L.; resources, C.L. and B.F.; data curation, H.C. and Q.L.; writing—original draft preparation, H.C.; writing—review and editing, B.F., C.L. and Z.L. (Zhenxing Li); visualization, H.C. and Z.L. (Zheng Liu); supervision, C.L.; project administration, C.L. and B.F.; funding acquisition, C.L. and B.F. All authors have read and agreed to the published version of the manuscript.

Funding: This research was funded by the China National Administration of Coal Geology National Science and Technology Major Project "Research on Prospecting and Development Technology of Deep Geothermal Resources" (Grant No. ZMKJ-2025-ZX02-2); and the Engineering Research Center of Geothermal Resources Development Technology and Equipment, Ministry of Education, Jilin University.

Data Availability Statement: The data supporting the results of this study are available in the manuscript. Processed analytical datasets can be obtained from the corresponding author upon reasonable request.

Acknowledgments: The authors appreciate the financial support from the China National Administration of Coal Geology National Science and Technology Major Project "Research on Prospecting and Development Technology of Deep Geothermal Resources" (Grant No. ZMKJ-2025-ZX02-2), and experimental materials, consumables, academic guidance, equipment support provided by the Engineering Research Center of Geothermal Resources Development Technology and Equipment, Ministry of Education, Jilin University. During the preparation of this manuscript, the authors used Doubao and Deepseek for language polishing and format adjustment. The authors have reviewed and edited all outputs and take full responsibility for the content of this publication. The authors appreciate the technical support and discussion provided by the research group. The authors thank the reviewers and editors for their valuable comments to improve this manuscript.

Conflicts of Interest: The authors declare no conflicts of interest.

Abbreviations

The following abbreviations are used in this manuscript:

TOUGHREACT	Non-isothermal multiphase reactive geochemical transport simulator
CV	Coefficient of variation
mD	millidarcy

References

1. Ju, F.; Guo, Z.; Yan, D.; Guo, M.; Chang, T.; Lin, Y.; Li, C. Brief analysis on sustainable development mode of geothermal resources under the "Green Beijing" strategy. *China Min. Mag.* **2015**, *24*, 07204. (In Chinese)
2. Sanyal, S.K.; Enedy, S.L.; Brophy, P.; Voge, E. The Geysers: The Oldest and Largest Geothermal Power Operation in the US. In *Geothermal Power Generation*; Elsevier Science Ltd.: Cambridge, MA, USA, 2025; pp. 689–709.
3. Hu, J.; Liu, Y.; Wang, X.; Zhang, Y.; Wei, M. Progress and Prospect of Mid-Deep Geothermal Reinjection Technology. *J. Groundw. Sci. Eng.* **2024**, *12*, 321–338. [CrossRef]
4. Mas, P.; Calcagno, P.; Caritg-Monnot, S.; Beccaletto, L.; Capar, L.; Hamm, V. A 3D Geomodel of the Deep Aquifers in the Orléans Area of the Southern Paris Basin (France). *Sci. Data* **2022**, *9*, 781. [CrossRef] [PubMed]
5. Castillo, C.; Kervévan, C.; Thiéry, D. Geochemical and Reactive Transport Modeling of the Injection of Cooled Triassic Brines into the Dogger Aquifer (Paris Basin, France). *Geothermics* **2015**, *53*, 446–463. [CrossRef]
6. Guo, Y.; Xu, Y.; Wang, H.; Shen, J.; Zhao, S. Experimental Investigation of Water-Rock Reaction for the Reinjection of Sandstone Geothermal Reservoirs: A Case from Neogene Guantao Formation in Tianjin. *Renew. Energy* **2023**, *210*, 203–214. [CrossRef]
7. Xia, J.; Tian, H.; Dou, B.; Xiao, P.; Zheng, J.; Lai, X. Experimental Review: Particle Clogging in Porous Sandstone Geothermal Reservoirs during Tail Water Reinjection. *J. Hydrol.* **2023**, *625*, 130066. [CrossRef]
8. Huang, G.; Hu, X.; Liu, L.; Liu, S.; Peng, R.; Yang, J. Geothermal resource evaluation under non-homogeneous thermal reservoir properties in Xiong'an New Area. *Earth Sci.* **2024**, *49*, 4576–4593. (In Chinese) [CrossRef]
9. Qiu, J.; Xin, Y.; Shao, B.; Liu, Z. Development law of karst fractures in Wumishan Formation thermal reservoir in southern plain area of Tianjin. *China Geol. Surv.* **2023**, *10*, 81–88. [CrossRef]
10. Li, H.; Li, J.; Ruan, C.; Liu, Z.; Chen, Y.; Du, F. Hydrogeochemical Processes and Thermal Mechanisms of Deep-Buried Uplift Dolostone Reservoirs in the North China Basin. *Geothermics* **2026**, *141*, 103766. [CrossRef]
11. Yang, M.; Liu, P.; Wang, J.; Feng, D.; Guo, G.; Yang, J.; Xiong, X.; Xie, D.; Wang, H. The Simulation of Hydrogeochemical Responses to Multi-Source Injection in Carbonate Geothermal Reservoir-a Case Study of Wumishan Formation (Jxw) from Beijing. *Ecol. Front.* **2026**, *46*, 1873–1886. [CrossRef]
12. Shi, J.; Yang, Y.; Lu, Y.; Li, S.; Zhang, W.; Wang, L.; Ding, X.; Zhu, Y. Hydrochemical Evolution and Environmental Implications of Geothermal Reservoirs Under Transient Surface Water Injection. *J. Environ. Manag.* **2026**, *401*, 128735. [CrossRef] [PubMed]

13. Li, S.; Wen, D.; Feng, B.; Li, F.; Yue, D.; Zhang, Q.; Wang, J.; Feng, Z. Numerical optimization of geothermal energy extraction from deep karst reservoir in north China. *Renew. Energy* **2023**, *202*, 1071–1085. (In Chinese) [CrossRef]
14. Xu, D.; Liu, J.; Liang, C.; Lin, H.; Zhou, L.; Zhao, C.; Zhang, L. Fracture Surface Morphology Effect on Radial Seepage Flow in a Horizontal Single Granite Fracture. *Bull. Eng. Geol. Environ.* **2024**, *83*, 55. [CrossRef]
15. Xu, D.; Liu, J.; Liang, C.; Yang, J.; Xu, H.; Wang, L.; Liu, J. Effects of Cyclic Fatigue Loads on Surface Topography Evolution and Hydro-Mechanical Properties in Natural and Artificial Fracture. *Eng. Fail. Anal.* **2024**, *156*, 107801. [CrossRef]
16. Yang, Y.; Li, L.; Wen, T.; Shen, L.W.; Chen, E.J.; Dong, X.; Xu, J. Distinguishing Rock Fracture and Pore's T2 Signals from NMR Experiments with Assisted X-ray CT Imaging. *Energy Sci. Eng.* **2025**, *13*, 4178–4189. [CrossRef]
17. Vogler, D.; Walsh, S.D.C.; Bayer, P.; Amann, F. Comparison of Surface Properties in Natural and Artificially Generated Fractures in a Crystalline Rock. *Rock Mech. Rock Eng.* **2017**, *50*, 2891–2909. [CrossRef]
18. Achuo Dze, S.; Phillips, T.; Najafi-Silab, R.; Perez, S.; Bultreys, T.; Novak, V.; Schlepütz, C.M.; Cnudde, V.; Doster, F.; Singh, K.; et al. Analysis and Comparison of Natural Shear and Induced Tensile Fractures for Caprock Leakage Assessment. *Transp. Porous Media* **2026**, *153*, 29. [CrossRef] [PubMed]
19. Turbakov, M.S.; Shcherbakov, A.A.; Riabokon, E.P.; Ivanov, Z.G.; Kamenev, P.A.; Kazymov, K.P.; Tomilina, E.M.; Pshevlodskii, M.A.; Shcherbakova, Y.S.; Kozhevnikov, E.V. Stress-Dependent Permeability of Artificially Fractured Siliceous Rocks from Southern Sakhalin. *Geosciences* **2026**, *16*, 358. [CrossRef]
20. Wang, T.; Xiang, K.; Tong, X.; Yan, L. Upscaling Spectral Induced Polarization from Pore to Core Scale in Tight Reservoirs: A 3D Impedance Network Approach with an Improved Membrane Polarization Model. *Minerals* **2026**, *16*, 766. [CrossRef]
21. Guo, X. Investigation of the Temperature Effect on Rock Permeability Sensitivity. *J. Pet. Sci. Eng.* **2017**, *156*, 616–622. [CrossRef]
22. Wu, J. A new method for investigating the impact of temperature on in-situ reservoir properties using high-temperature AFM. *Geothermics* **2024**, *120*, 103006. [CrossRef]
23. Pei, L.; Blöcher, G.; Milsch, H.; Zimmermann, G.; Sass, I.; Li, X.; Huenges, E. Response of Upper Jurassic (Malm) Limestone to Temperature Change: Experimental Results on Rock Deformation and Permeability. *Rock Mech. Rock Eng.* **2021**, *54*, 337–358. [CrossRef]
24. Gao, J.; Wang, Y.; Wang, C. Study on porosity and permeability characteristics of carbonate rocks in Shaanxi-Gansu-Ningxia basin. *Acta Pet. Sin.* **1996**, *17*, 64–70. (In Chinese)
25. She, M.; Shou, J.; Shen, A.; Pan, L.; Hu, A.; Hu, Y. Experimental simulation of dissolution law and porosity evolution of carbonate rock. *Pet. Explor. Dev.* **2016**, *43*, 616–625. [CrossRef]
26. Lin, T.; Wang, T.; Dong, J.; Zeng, Y.; Wu, Z. Characteristics of permeability mechanical behavior of typical carbonate rocks and its identification for reservoir and caprock properties. *Nat. Gas. Geosci.* **2020**, *31*, 1139–1151. (In Chinese) [CrossRef]
27. Liu, D.; Cai, Y.; Feng, Z.; Zhang, Q.; Hu, L.; Li, S. Feasibility Study on Geothermal Dolomite Reservoir Reinjection with Surface Water in Tianjin, China. *Water* **2024**, *16*, 3144. [CrossRef]
28. Chai, R.; Liu, Y.; Xue, L.; Rui, Z.; Zhao, R.; Wang, J. Formation Damage of Sandstone Geothermal Reservoirs: During Decreased Salinity Water Injection. *Appl. Energy* **2022**, *322*, 119465. [CrossRef]
29. Yang, J.; Tao, Y.; Gao, Y.; Wang, L.; Kang, B. Experimental Study on the Water-Rock Interaction Mechanism in a Groundwater Heat Pump Reinjection Process. *J. Water Clim. Change* **2022**, *13*, 1516–1533. [CrossRef]
30. Sendula, E.; Albrecht, R.; Conceição de Castro, C.; Keresztény-Borbás, E.; Szabó-Krausz, Z.; Kovács, J. Characteristics of Heat-Depleted Thermal Water Re-Injection-Induced Water–Rock Interactions in a Sandstone Reservoir Containing Carbonate and Silicate Minerals (Szentes, Hungary). *Minerals* **2025**, *15*, 513. [CrossRef]
31. Huang Investigations of the impact of geothermal water reinjection on water-rock interaction through laboratory experiments and numerical simulations. *Appl. Geochem.* **2024**, *175*, 106180. [CrossRef]
32. Wang, B.; Zhao, Y.; Cai, Y.; Zhang, S.; Yang, B.; Liu, F. Feasibility Research on Surface Water Reinjection into the Sandstone Geothermal Reservoir of the Guantao Formation in Tianjin Based on Laboratory Experiments. *Water* **2024**, *16*, 2475. [CrossRef]
33. Zhao, M.; Xiaochong, D.; Shanfeng, Q.; Min, J.; Guangxu, B.; Xin, T.; Zhongfeng, D. Numerical Simulation of Hydrochemical Evolution of Deep Pore Thermal Reservoirs in Shallow Groundwater Recharge of Yancheng Uplift. *Sci. Rep.* **2025**, *15*, 39538. [CrossRef] [PubMed]
34. Liu, Z.; Feng, B.; Alexey, K.; Shen, J.; He, S.; Yuan, Y. Impact of Injected Water Chemistry on Mineral Precipitation and Dissolution in Medium–Deep Geothermal Systems: A Case Study of the Wumishan Formation Dolomite Reservoir. *Water* **2025**, *17*, 3099. [CrossRef]
35. Liu, B.; Jing, W.; Long, D.; Li, J.; Ding, D.; Cai, K. Long-Term Simulation of Process and Hydrogeochemistry of Gas Field Produced Water Reinjection into a Limestone Reservoir. *Phys. Chem. Earth Parts ABC* **2025**, *139*, 103976. [CrossRef]
36. Altar, D.E.; Kaya, E.; Zarrouk, S.J.; Chambefort, I. Natural State Geothermal Reservoir Modelling: Mineralogical and Geochemical Evolution Perspective. *Geothermics* **2024**, *123*, 103132. [CrossRef]
37. Todaka, N.; Spycher, N.; Kowalsky, M.B.; Finsterle, S.; Shimizu, S.; Sakai, T.; Nakanishi, S. Thermal-Hydrological-Geochemical Modeling of the Distribution of Acidic Fluids at the Onikobe Geothermal Field, Japan. *Geothermics* **2025**, *130*, 103308. [CrossRef]

38. Bett, G.; Yasuhiro, F. Integrated Geological Assessment and Numerical Simulation for Olkaria's East and Southeast Geothermal Fields. *Geothermics* **2023**, *109*, 102652. [CrossRef]
39. Liu, H.; Gao, L.; Zhang, J.; Hou, H.; Xie, M.; Li, H. Bedrock surface and fault structures in the Rongcheng Bulge revealed from reflection seismic profiles and their implications for the geothermal origin. *Geophys. Geochem. Explor.* **2024**, *48*, 934–944. (In Chinese) [CrossRef]
40. Guo, R.; Ji, Y.; Ma, Z.; Wan, H.; Yang, D.; Ji, H.; Bao, Z.; Zhou, Y.; Fang, C.; Lu, K.; et al. Reservoir-forming mechanism and development model of karst geothermal reservoir of Wumishan Formation in Xiong'an New Area. *J. Palaeogeogr. (Chin. Ed.)* **2023**, *25*, 180–197. (In Chinese) [CrossRef]
41. Ma, F.; Wang, G.; Yu, M.; Zhu, X. Physical property characteristics and productivity analysis of carbonate geothermal reservoir in Rongcheng geothermal field, Xiong'an New Area. *Contrib. To Geol. Mineral. Resour. Res.* **2026**, *41*, 1–13. (In Chinese) [CrossRef]
42. Dai, M.; Sun, P.; Lei, H.; Xing, Q.; Bao, Z. Stratigraphy and structural characteristics of main geothermal reservoir spaces and geothermal water resource potential in Xiong'an New Area. *Chin. J. Geol.* **2023**, *58*, 412–437. (In Chinese) [CrossRef]
43. Lu, K.; Bao, Z.; Ji, H.; Liu, J.; Wang, G.; Ma, F.; Guo, R.; Cao, Y.; Yang, F.; Fu, Y.; et al. Characteristics, main controlling factors and favorable zone prediction of karst geothermal reservoir of Wumishan Formation (Jixian System) in Xiong'an New Area. *J. Palaeogeogr. (Chin. Ed.)* **2019**, *21*, 885–900. (In Chinese) [CrossRef]
44. Wang, Z.; Zhang, C.; Jiang, G.; Hu, J.; Tang, X.; Hu, S. Present-day geothermal field characteristics and genetic mechanism in Xiong'an New Area. *Chin. J. Geophys.* **2019**, *62*, 4313–4322. (In Chinese) [CrossRef]
45. Yang, S.; Huang, H.; Song, D.; Wang, C.; Zhang, Y.; Yan, P. Design and application of electric control system for geothermal recharging water treatment. *Ind. Instrum. Autom.* **2026**, 3–8. (In Chinese) [CrossRef]
46. Cobos, J.E.; Søgaard, E.G. Systematic Study of Geothermal Brine Reinjection for SaltPower Generation Purposes: Citric Acid as a Potential Iron Control Agent. *Geothermics* **2021**, *95*, 102116. [CrossRef]
47. Abdulagatov, I.M.; Akhmedova-Azizova, L.A.; Aliev, R.M.; Badavov, G.B. Measurements of the density, speed of sound, viscosity and derived thermodynamic properties of geothermal fluids from south russia geothermal field. Part II. *Appl. Geochem.* **2016**, *69*, 28–41. [CrossRef]
48. Fan, Y.L.; Tan, C.X.; Zhang, P.; Sun, M.Q.; Qi, B.S.; Feng, C.J.; Meng, J.; Wang, H.Q. A study of current in-situ stress state and its influence on tectonic stability in the Xiongan New Area. *Acta Geosci. Sin.* **2020**, *41*, 481–491. (In Chinese) [CrossRef]
49. Yousefi, M.; Dehghanpour, H. A Model and Measurement Technique for Liquid Permeability of Tight Porous Media Based on the Steady-State Method. *Energy Fuels* **2022**, *36*, 6860–6867. [CrossRef]
50. Khani Rasmussen, S.; Al-Masri, W.F.; Rostami, B.; Olsen, D.; Nielsen, C.M. Steady-StateCO_2–Brine RelativePermeability and Hysteresis in Stenlille Sandstone. *Energy Fuels* **2026**, *40*, 18350–18369. [CrossRef]
51. Fu, L.P.; Mu, Z.H.; Zhang, G.C.; Li, X.R. A study of reservoir heterogeneity based on petrophysical facies: A case from Qie 12 well block of Kunbei Oilfield. *Geol. Sci. Technol. Inf.* **2018**, *37*, 114–119. (In Chinese) [CrossRef]
52. Tang, B.N.; Zhu, C.Q.; Qiu, N.S.; Cui, Y.; Guo, S.S.; Chen, C. Karst fracture development characteristics of the Wumishan Formation in the Xiongan New Area. *Acta Geol. Sin.* **2020**, *94*, 2002–2012. [CrossRef]
53. Witherspoon, P.A.; Wang, J.S.Y.; Iwai, K.; Gale, J.E. Validity of Cubic Law for Fluid Flow in a Deformable Rock Fracture. *Water Resour. Res.* **1980**, *16*, 1016–1024. (In Chinese) [CrossRef]
54. Xu, T.; Sonnenthal, E.; Spycher, N.; Pruess, K. TOUGHREACT—A Simulation Program for Non-Isothermal Multiphase Reactive Geochemical Transport in Variably Saturated Geologic Media: Applications to Geothermal Injectivity and CO_2 Geological Sequestration. *Comput. Geosci.* **2006**, *32*, 145–165. [CrossRef]

Disclaimer/Publisher's Note: The statements, opinions and data contained in all publications are solely those of the individual author(s) and contributor(s) and not of MDPI and/or the editor(s). MDPI and/or the editor(s) disclaim responsibility for any injury to people or property resulting from any ideas, methods, instructions or products referred to in the content.